공학박사학위논문

결정 경계와 구멍 결함에 의한
다결정 CVD 그래핀의 열전도도 감소

Thermal Conductivity Reduction of Polycrystalline CVD

Graphene by Grain Boundary and Hole Defect

2018 년 8 월

서울대학교 대학원

기계항공공학부

이 우 민

Thermal Conductivity Reduction of Polycrystalline CVD Graphene by Grain Boundary and Hole Defect

Woomin Lee

School of Mechanical and Aerospace Engineering

Seoul National University

Abstract

Graphene, a two-dimensional material consisting of carbon atoms, has attracted great interest due to its novel physical properties, such as high electrical mobility, optical transparency, and superior mechanical strength. Especially, graphene has exceptionally outstanding thermal properties owing to long mean free path of phonon in two-dimensional lattices. The extraordinarily high thermal conductivity of graphene can be remarkably reduced by some defects, such as grain boundary, vacancy, and foreign atom. Therefore, Grain boundary effects on thermal transport in CVD grown graphene that has many grain boundaries should be investigated.

In this study, graphene samples with different grain sizes were synthesized by chemical vapor deposition (CVD) system to investigate the grain boundary effect on thermal transport in polycrystalline graphene. Manipulation of the CVD

synthesis conditions allowed for synthesis of polycrystalline single-layered graphene with controlled grain sizes. Thermal conductivities of 3 graphene with different grain sizes were measured by the optothermal Raman technique, using the temperature-dependent $2D$ peak shift in Raman spectra. At first, the optical absorption was measured to define the absorbed power of defected graphene by Raman laser irradiation. Then, the temperature coefficient of Raman $2D$ peak positions and $2D$ peak shifts as the absorbed power were measured. Finally, thermal conductivities of defected graphene were obtained by solving the heat diffusion equation where experimental data were used. Furthermore, the effect of air convection losses and the hole edge temperature of suspended graphene were analyzed by numerically solving the full energy balance. Thermal conductivities of the single-crystal graphene as temperature were estimated by extrapolation/fitting of the experimental data. And the temperature discrepancies between the measured temperature from G peak and $2D$ peak shifts were compared to confirm noneuqilibrium phonons.

Although defects in graphene have a detrimental effect on thermal conductivity of graphene, the thermal conductivity suppression of graphene by defects can be useful for various applications. For the quantitative study of thermal conductivity of graphene as defects concentrations and for the more effective thermal conductivity suppressions, thermal conductivity reductions of holey graphene (HG)

as porosity were measured by optothermal Raman method. HG samples were obtained by focused ion beam (FIB) processing for the study. The hole defects were precisely fabricated and controlled by direct FIB milling which does not require any masking or post processing. After graphene samples were transferred on the substrate by PMMA, all samples were characterized by diverse technique (e.g. Raman spectroscopy, SEM, optical microscope) Finally, the measured thermal conductivity reductions of holey graphene as porosity were compared to other reference experimental data and calculation results.

Keywords: thermal conductivity, CVD graphene, optothermal Raman technique, grain boundary, holey graphene,

Student Number : 2013-20696

Contents

Chapter 3. *k* Reductions of Holey Graphene as Hole-Defect Porosity

List of Tables

List of Figures

Nomenclature

Roman symbols

a optical absorption (%)

c heat capacity (J/K)

G thermal conductance (W/m^{2}K)

h convection heat transfer coefficient (W/m^{2}K)

k thermal conductivity (W/mK)

l average grain size (m)

n number of experimental data

P transmitted power (W)

q'' heat flux (W/m^2)

q_0'' peak absorbed at the center of beam spot (W/m^2)

Q total laser power (W)

r radial distance from the origin of cylindrical coordinate system (m)

R suspended hole radius (m)

Re reflectance (%)

RE thermal resistance (m^{2}K/W)

r_0 Gaussian laser beam radius (m)

s standard deviation

t	thickness (m)
T	temperature (K)
Tr	transmittance (%)
U	uncertainty
v	phonon velocity (m/s)

Greek symbols

α	integral function of r_0 and R
ε	emissivity
λ	mean free path (m)
Λ	wavelength (m)
ρ	reflectance ratio (Re_g/Re_{SiO2})
σ	Stefan-Boltzmann constant (5.60×10^{-8} W/m^{2}k^4)
τ	transmittance ratio (Tr_g/Tr_{SiO2})
ω	Raman peak position (cm^{-1})

Subscripts

0	reference
2D	Raman 2D band
a	ambient

Ball   ballistic

D   Debye

empty   empty

G   Raman G band

g   graphene

GB   grain boundary

m_cal   measured by calculation

m_exp   measured by experiment

p   phonon

PG   pristine graphene

rad   radiation

sg   sigle-crystalline

sup   supported

sus   suspended

SiO_2 silicon dioxide substrate

Abbreviations

3-ω   3 omega

CVD   chemical vapor deposition

D.I.   deionized

FIB   focused ion beam

FWHM full width at half-maximum

GNM   graphene nanomesh

HE   hole edge

HG   holey graphene

$I(D)$ Raman D peak intensity

$I(2D)$ Raman $2D$ peak intensity

Inc.   incorporation

MD   molecular dynamics

MDA   mild dry annealing

MEMS microelectromechanical systems

MFC   mass flow controller

NA   numerical aperture

NE   nonequilibrium

SEM   scanning electron microscopy

Chapter 1

Introduction

1.1 Background

Graphene is one layer of carbon atoms in the form of a two-dimensional, hexagonal lattice. After it had been first produced in 2003 (Novoselov et al. 2004), research about graphene has been conducted actively by many extraordinary physical properties, such as high electrical mobility (Bolotin et al. 2008), optical transparency (Nair et al. 2008), superior mechanical strength (Lee et al. 2008), and novel thermal conductivity (Balandin et al. 2008). Based on the outstanding properties, graphene has great opportunities in various research fields like gas/bio sensors (Schedin et al. 2007), transparent electrodes (Kim et al. 2009), and battery (Gilje et al. 2007).

Graphene has higher thermal conductivity than any other materials due to long mean free path of phonon by strong carbon-carbon bonding in two-dimensional lattices (Balandin 2011; Nika et al. 2009). The measured thermal conductivity of suspended graphene is over 2000　W/mK　at room temperature, which is still higher than that of the bulk graphite (Balandin et al. 2008; Cai et al. 2010; Chen et al. 2010). However, the extraordinarily high thermal conductivity of graphene is

remarkably reduced by defects (Balandin 2011; Chen et al. 2012b; Malekpour et al. 2016). Therefore, it should be needed to experimentally probe the defect effects on thermal transport in defected graphene in order to complete understanding thermal physics for applications in thermal managing.

1.2 Review of previous studies

1.2.1 Polycrystalline CVD graphene

There are some methods to obtain graphene, such as mechanical exfoliation (Novoselov et al. 2004), epitaxial growth (Berger et al. 2006), and CVD system (Li et al. 2009) and each methods have some strong and weak points summarized in Table 1.1. CVD system is a very promising method among them, because large-area synthesis is available and capable of doping to control specific properties of graphene. In synthesis of CVD method, carbon atoms dissociated from the precursor gas are deposited on Cu foil forming the nucleation seeds. Then, the seeds grow up and the full-coverage graphene is synthesized by combining the respective grain islands. As a result, the graphene grown by CVD method is polycrystalline consisted of many grain domains. The grain boundaries between grain islands has critical effect on thermal transport in graphene by additional boundary scattering depicted in Figure 1.1. On the other hand, the grain size variation is expected to

enable more effective thermal transport control by including the grain boundary scattering effect in addition to size confinements. A number of theoretical studies evidenced the potential merit of grain size variation for thermal transport control; nonequilibrium Green's function theory showed the reduction of thermal conductivity by decreasing grain sizes for supported graphene (Serov et al. 2013), theoretical characterization of phonon transport in polycrystalline graphene found the thermal conductivity to increase with the grain size (Wang et al. 2014), and molecular dynamics simulation for the thermal transport behavior were performed to study the effect of grain size on the thermal conductivity of polycrystalline graphene (Wu et al. 2014). However, no study has been published that experimentally probed the grain size effect on thermal conductivity of polycrystalline graphene. Therefore, it is needed to study grain boundary effect on thermal conductivity of polycrystalline graphene.

1.2.2 Holey graphene with hole-shaped defects

It is obvious that defects have detrimental effect on thermal conductivity of graphene by additional defect scattering. Nevertheless, the defected graphene can be useful for various application area by nano-engineered defects to tailor the local properties of graphene achieving new functionalities (Banhart et al. 2010). Recently, many researchers have tried to reduce thermal conductivity by intentionally

fabricating defects in graphene for various application fields; the thermal conductivity of defective graphene by oxygen plasma treatment dropped to 17 % for 0.1 % defects and the asymmetric junction between pristine graphene and defective graphene showed a high thermal rectification ratio of 46 % (Zhao et al. 2015), and thermoelectric properties was enhanced by significantly reduced thermal conductivity of GNM with sub-10 nm neck-width (Oh et al. 2017). Although extensive works have been done on reducing the thermal conductivity of defective graphene, no study has been reported that experimentally probing quantitative changes of thermal conductivity by defects because it is hard to control accurate concentrations and sizes of defects in graphene. Holey graphene fabricated by FIB processing is suitable for the quantitative study of thermal conductivity changes by defects concentrations, because FIB drilling is high accuracy technique without any masking and post processing so the fabrications of hole defects can be controlled precisely. And hole defects effect on thermal transport in holey graphene can be investigated experimentally where hole defects will critically affect thermal conductivity by defect scattering depicted in Figure 1.2.

1.2.3 Thermal conductivity measurement of graphene

The thickness of graphene (0.335 nm) is too small, so it is impossible to measure thermal conductivity by general measurement technique using

thermocouple to know temperature. The confident thermal conductivity of supported graphene on SiO_2 was reported using micro-resistance thermometry (Seol et al. 2010), but micro resistance thermometry involves very complicated processing to prepare sample and have a difficulty to measure the thermal conductivity of suspended graphene to probe the intrinsic thermal transport. In contrast, optothermal Raman method is very simple which is unnecessary any complicated processing and effective to measure the thermal conductivity of suspended graphene. Also, optothermal Raman technique don't destroy graphene samples while conducting the measurement experiment, using the correlation between temperature and Raman peak center to know the increased graphene temperature by Raman laser irradiation, as shown in Figure. 1.3.

A lot of previous studies measuring thermal conductivity of graphene using optothermal Raman method have been reported due to many advantages. At first, Balandin et al. (2008) reported the thermal conductivity of suspended graphene as ~5000 W/mK at room temperature, which is slightly overestimated due to assumption to high optical absorption (Balandin et al. 2008). Then, thermal conductivities of graphene suspended on different hole sizes (Chen et al. 2010), isotopically modified graphene (Chen et al. 2012b), and graphene with wrinkles (Chen et al. 2012a) were measured by optothermal Raman method summarized in Table 1.2. Consequently, optothermal Raman method is used to measure the

thermal conductivities of all samples despite of low accuracy in this study.

1.3 Objective of the present study

As mentioned in previous sections, there are few studies to experimentally investigate defect effects on thermal transport in defected graphene. In this thesis, a study on thermal properties of defected graphene by optothermal Raman method was conducted. This result should be needed to fully understand thermal transport in defected graphene and shed light on a possibility in various application fields of defected graphene.

In Chapter 2, it is presented grain boundary effects on thermal transport in polycrystalline CVD graphene. In order to figure out the grain boundary effects, 3 graphene samples with different grain sizes were synthesized by manipulating synthesis conditions in CVD system. After graphene samples were transferred on a thorough hole to avoid substrate effect by PMMA transfer method, all samples are characterized by optical microscopy, SEM, and Raman spectroscopy before measuring thermal conductivity. After briefly introducing optothermal Raman method, the optical absorption of graphene, the correlation between $2D$ peak positons and temperature, and the temperature rises as the absorbed laser power are presented. Finally, the obtained thermal conductivities of defected graphene are

discussed. Furthermore, experimental results are analyzed. First of all, the uncertainties of the measured thermal conductivities are estimated by root-sum-square method (Moffat 1988). Then, hole edge temperature of suspended graphene and the effect of air convection losses are calculated by numerically solving the full heat diffusion equation. Also, the thermal conductivities of single-crystal graphene as temperature is estimated by extrapolation and fitting of the experimental data. And Temperature discrepancies measured from G peak and $2D$ peak shifts by nonequilibrium phonons are compared to confirm the degree of nonequilibrium phonons.

In Chapter 3, thermal conductivity reductions of holey graphene as porosity is covered for the quantitative study on thermal conductivity of defected graphene as defect concentrations. Hole defects in polycrystalline graphene were fabricated by FIB processing. Then, characterizations were conducted about the holey graphene using the same methods as mentioned in Chapter 2. Finally, the measured thermal conductivity reductions were compared to other reference data.

Finally, summary and conclusion are presented in Chapter 4.

Table 1.1 Comparison of graphene production methods including principle, strong point, and weak point about respective method

Methods	Pros	Cons
CVD Deposition of carbon source gas at high temperature	Large size sample Easy to produce Capable of doping	Reaction residuals Polycrystalline
Exfoliation Peeling of graphite crystal by cellophane tape	Easy to produce High quality	Small size sample Tape residuals
Epitaxial growth Sublimation of Si from silicon carbide	Very clean synthesis	High temperature Ultrahigh vacuum
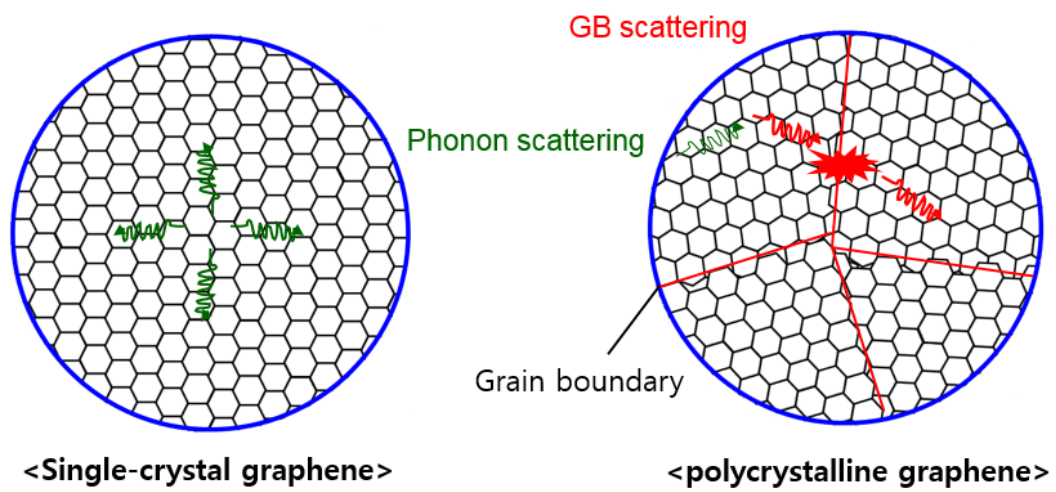
Figure 1.1 Schematic of phonon scattering in single-crystal graphene and polycrystalline graphene. The phonon-phonon scattering is dominant in single-crystal graphene. There are additional grain boundary scattering in polycrystalline graphene
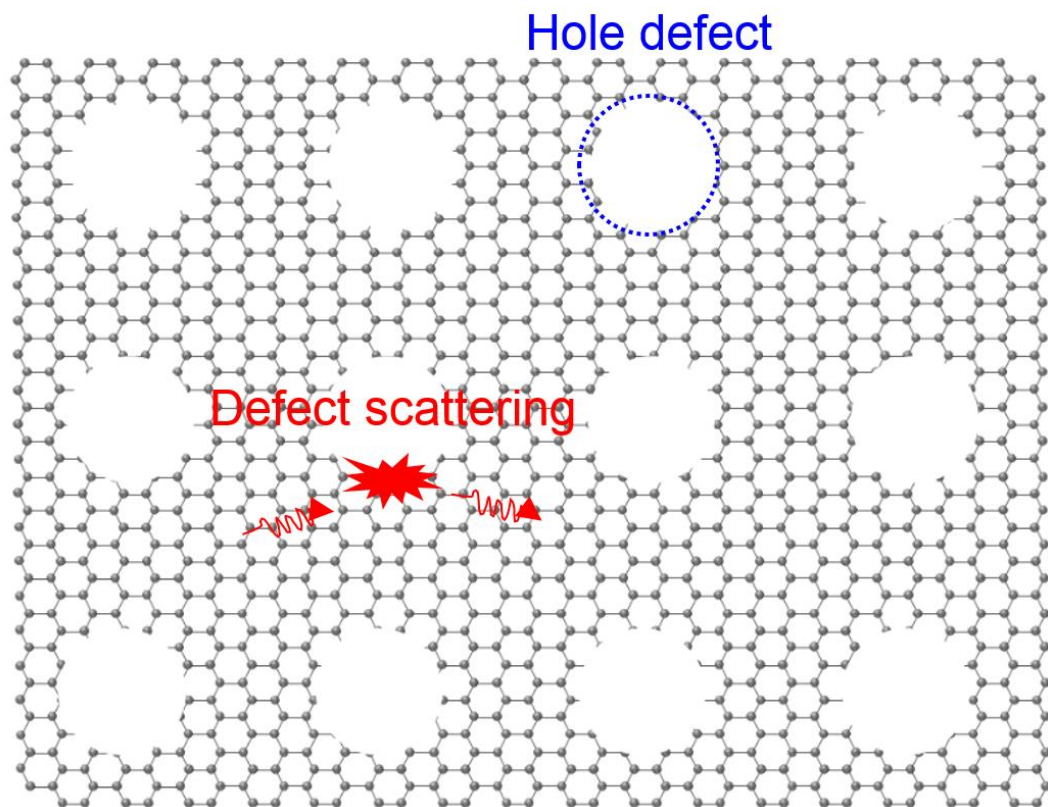
Figure 1.2 Schematic of phonon scattering in holey graphene. Imperfect bonding like dangling bonding around hole defects enhance defects scattering in addition to phonon-phonon scattering
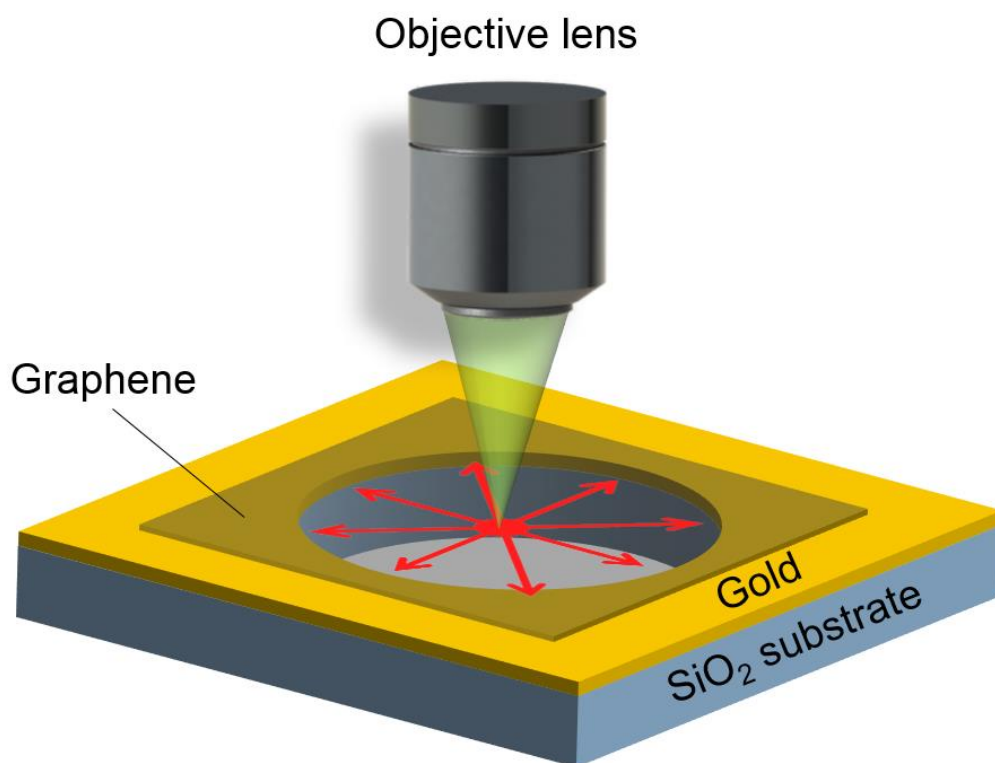
Figure 1.3 Schematic of optothermal Raman method. The increased graphene temperature by Raman laser irradiation is measured by correlation between temperature and Raman peak center

Table 1.2 Summary of k measurement of graphene

Sample	k [W/mK] at RT	Method	Reference	Remarks
Exfoliated graphene	~5000	Optothermal Raman	Balandin et al. 2008	- Suspended on trench - The first k measurement of graphene - Overestimated α : 13 % - Plane wave heat propagation
Exfoliated graphene	600	Micro-resistance thermometry	Seol et al. 2010	- Supported on SiO_2 substrate - High accuracy - Low temperature ranges : 80 ~ 400 K
CVD graphene	2200 ~ 3000	Optothermal Raman	Chen et al. 2010	- Suspended on different hole sizes - h : 2.9×10^4 W/m^{2}K - Cylindrical heat propagation
CVD graphene	2900 without wrinkle 2000 with wrinkle	Optothermal Raman	Chen et al. 2012a	- Suspended on hole - k comparison of graphene with wrinkle and without wrinkle
CVD graphene	4000 (0.01% ^{13}C) 2800 (1.1, 99.2% ^{13}C) 2200 (50% ^{13}C)	Optothermal Raman	Chen et al. 2012b	- Suspended on hole - k of isotopically modified graphene - Physical elaboration by MD

Chapter 2

Grain Size Effects on *k* of Polycrystalline graphene

2.1 Introduction

In this chapter, sample preparation and characterization of 3 graphene samples with different grain sizes will be presented. By manipulating the synthesis conditions in CVD system, grain sizes of polycrystalline graphene will be synthesized. Each samples will be transferred on a through hole substrate by PMMA transfer method. Then, the graphene samples will be confirmed by various technique, such as SEM, optical microscopy, and Raman spectroscopy. And the grain sizes of polycrystalline CVD graphene samples will be defined. Finally, grain boundary effects on thermal transport in polycrystalline graphene are investigated by measuring thermal conductivities of polycrystalline graphene with different grain sizes. Furthermore, the experimental results are elaborated by analyzing measurement uncertainties and calculating hole edge temperature, convection loss. Also, thermal conductivities of single-crystal graphene are obtained by extrapolation of the measured experimental data and temperature discrepancies between temperatures from Raman G peak and $2D$ peak shifts are compared to confirm the local nonequilibrium of phonons.

2.2 Sample preparation

In this chapter, sample preparation and characterization of all samples will be presented. By manipulating the synthesis conditions in CVD system, grain sizes of polycrystalline graphene will be synthesized. Graphene samples will be transferred on a substrate with a through hole of 8 μm by PMMA transfer method. Then, the graphene samples will be confirmed by various technique, such as SEM, optical microscopy, and Raman spectroscopy. Finally, the grain sizes of graphene samples will be defined.

2.2.1 Control of the grain sizes of polycrystalline graphene

In order to probe grain boundary effect on thermal transport in polycrystalline graphene, graphene samples with different grain sizes should be needed. In CVD system, manipulation of CVD synthesis conditions, such as partial pressure, synthesis temperature, synthesis time, and precursor gas concentration ratios, allowed for synthesis of polycrystalline single-layered graphene with controlled grain sizes. Therefore, a low-pressure-high-temperature chemical vapor deposition system was used to obtain graphene samples.

Figure 2.1 shows the experimental setup of CVD system (ScienTech Inc.) used in this experiment. In this CVD system, hydrogen, methane, and argon gas can be

supplied for graphene synthesis where methane is a precursor gas containing carbon atoms. The flow rate of gases is elaborately controlled by MFC. The temperature in furnace and gas flow rate is controlled by main system controller. The pressure in the quartz tube is checked by the pressure sensor and is maintained about 10^{-4} torr by the vacuum pump when there aren't any gas flow. Finally, the attenuated gases after passing the gas scrubber is exhausted to atmosphere.

In this CVD method, a catalyst should be needed for deposition of carbon species associated from a precursor gas at high temperature. Low carbon solubility of copper is favorable to grow the single-layered graphene, while graphene used nickel as catalyst shows spatially nonuniform and multi-layer (Li et al. 2009). Therefore, copper foils (25 μm thick, 99.999 % purity by Alfa Aesar Inc.) was used as catalyst for large single-layered graphene.

During the initial growth stage of graphene, both lower synthesis temperatures and higher methane flow rates allow denser nucleation of carbon atoms (Lewis et al. 2013; Li et al. 2010; Eres et al. 2014; Celebi et al. 2011); thus proper combination of these conditions can create CVD graphene specimens with variable grain sizes as summarized in Table 2.1 where the definition of grain sizes will be presented in Section 2.3.3 in detail. Each of the synthesis recipes for both 4.1 and 2.2 μm grain consists of double steps: (1) the initial low CH_4:H_2 ratio reduces the initial nucleation density to allow the grain islands to grow slowly into relatively larger

grains (Li et al. 2010) and (2) the higher $CH_4:H_2$ ratio of step 2 provides a sufficient amount of hydrocarbon radicals for full coverage beyond the island boundaries (Lewis et al. 2013).

As a result, three graphene samples with different grain sizes were obtained by manipulation of synthesis conditions in CVD system. By measuring the thermal conductivity of graphene samples with different grain sizes, the grain boundary effect on thermal transport in polycrystalline graphene will be studied experimentally.

2.2.2 Graphene transfer (the suspended graphene)

The transfer process is essential in order to conduct experiment of graphene sheet on copper foil after CVD synthesis. The PMMA is very helpful for graphene transfer, because the damage of graphene sheet can be protected during the transfer process and it is easy to handle by the coated PMMA onto graphene sheet.

The order of PMMA transfer is summarized in Figure 2.2. At first, PMMA solution is made by dissolving poly(methyl methacrylate) (average *Mw* ~996000 by GPC, Sigma-Aldrich product no.182265) in chlorobenzene with a concentration of 46 mg/mL and is kept on stirrer more than 2 days. Graphene on copper is spin coated (45 sec at 4000 rpm) by PMMA and heated at 160℃ for 90 sec to handle and preserve the graphene sheet.

Since graphene grows both sides of copper foil, 'back etching' is needed to remove the unnecessary graphene grown on the one side of copper foil. The back side of copper foil is etched by deionized water 15 minutes later after immersed in copper etchant which is the solution of 500 ml of deionized water (D.I. water) and 10 g of ammonium peroxydisulfate ($H_8N_2O_8S_2$). This process is repeated twice. The copper foil is entirely removed immersed in copper etchant during ~3 hour.

Then, PMMA + graphene is rinsed by D.I. water to clean out the copper etchant during 30 minutes. The floating PMMA/graphene on D.I. water is scooped up by the target substrate. The PMMA /graphene/substrate is dried in air (1 hour) and vacuum (1 hour) to remove the captured D.I water between graphene and substrate. Finally, graphene on the target substrate is obtained after PMMA is etched by acetone during 1 hour.

The graphene samples with different grain sizes were transferred via upper mentioned PMMA spin-coating/etching process onto the 8 μm hole patterns that were made by MEMS process including the deep reactive-ion etching (DRIE) and wet etching of a silicon-nitride (Si_3N_4) substrate as shown in Figure 2.3. A thin Au (0.1 μm) / Cr (10 μm) layer was sputtered on the substrate to increases the contact conductance of the suspended graphene layer. The hole diameter (D) was selected to be an order-of-magnitude larger than the typically known mean-free-path λ_p~775 nm for acoustic phonons at room temperature ($1/K_n = D / 2 \lambda_p \sim 5.2$) (Ghosh et al.

2008b), ensuring that the hole size is sufficiently large that the incident Gaussian laser heat absorbed at the center region of the suspended graphene can be assumed to transfer to the hole edge almost entirely by diffusion. Also, the selected hole size is at least twice larger than the largest grain sizes of tested grain samples so that the grain size and boundary effects can be properly included in thermal conductivity measurements.

2.3 Characterization

The graphene sample on the substrate is characterized by various technique before conducting the main experiment. Basically, scanning electron microscopy (SEM) and optical microscopy is useful to confirm the quality of surface visually. However, the grain boundaries are not visible without any treatment. Therefore, the grain boundaries are visualized by mild dry annealing (MDA) and the average grain sizes are defined by digital image processing.

2.3.1 Scanning electron microscopy (SEM)

In general, the resolution of SEM is much higher than that of optical microscope. Therefore, SEM image is used in a lot of field of research. In this study, SEM images are used to confirm the initial nucleation density and the coverage of

graphene. As presented in Section 2.2.1, many synthesis conditions were tried to obtain graphene samples with different grain sizes. In particular, the synthesis temperature and partial pressure of precursor have the critical effects on the initial nucleation density which is the key factor to conclude the grain sizes. Figure 2.4 shows that the nucleation density increases with decreasing synthesis temperature and increasing partial pressure of precursor. (Note that the images were taken at the prematurely grown CVD stage only to visibly confirm the different nucleation densities under different synthesis conditions.)

Figure 2.5 shows SEM image of the fully-grown graphene by CVD system. In this SEM image, the grain boundaries of copper are visible, but the grain boundaries of graphene are not visible. Therefore, it should be needed a certain treatment to visualize the grain boundaries of graphene. It will be presented in Section 2.3.3.

2.3.2 Optical microscopy

Optical microscopy is very simple and basic technique to confirm the experimental samples. Figure 2.6 shows optical images (100×0.75 NA objective lens) of the suspended graphene on 8 μm diameter patterned holes on a silicon-nitride (Si_3N_4) substrate. While the graphene samples have different grain sizes of 4.1, 2.2, and 0.5 μm respectively, all suspended graphene samples on the hole seem like black circle in Figure 2.6. Therefore, additional technique is needed to confirm

whether the graphene sheets is suspended on the hole or not, such as Raman spectroscopy. Nevertheless, the optical images around the hole is very clean, indicating the quality of graphene sheets is good without any noticeable defects.

2.3.3 Definition of grain sizes

As mentioned in previous sections, grain boundaries of the fully-grown CVD graphene cannot be detected by optical microcopy or SEM images. Therefore, it was tried to visualize the grain boundaries of graphene with different grain sizes by MDA. MDA (Lai et al. 2014) allows for visibility in Figure 2.7, owing to the fact that oxygen molecules readily penetrate the defects of grain boundaries to oxidize the copper substrate beneath along the grain boundaries (Larciprete et al. 2012). The digitally enhanced contrast further clarifies the grain boundaries in Figure 2.8 and the proper image analysis provides both the grain size distributions and their average values in Figure 2.9. As a result, the average grain sizes of graphene samples are 4.1, 2.2, and 0.5 μm.

2.3.4 Raman spectroscopy

Raman spectroscopy is very powerful technique to characterize conditions and quality of graphene (Ferrari and Basko 2013b). Raman spectrum of graphene has two distinctive peaks that is G peak and $2D$ peak. G peak ($\sim$1580 cm^{-1}) which is

common to all sp^2 carbon systems is given by the stretching of the C-C bond in graphitic materials (Dresselhaus et al. 2010). 2D peak (~2700 cm^{-1}) is a second-order process related to a phonon near the K point in graphene, activated by double resonance processes (Saito et al. 2001; Jiang et al. 2007). The presence of disorder in sp^2-hybridized carbon systems leads to rich and intriguing phenomena in their resonance Raman spectra, thus making D peak (~1350 cm^{-1}) (Ferrari 1824; Pimenta et al. 2007). Therefore, *D* peak is widely used to identify disorder in graphene.

At first, graphene samples with different grain sizes were probed by Raman spectroscopy. In Figure 2.10, the distinctive *G* peak and 2*D* peak of the Raman spectra, together with their peak ratio of $I(2D)/I(G) \sim 3.0$, depict the typical footprint (Ferrari and Basko 2013a; Berciaud et al. 2008) of single-layer graphene (Ferrari 2007a). Also, a more pronounced *D* peak is observed with decreasing grain size showing higher $I(D)/I(G)$ in Figure 2.11, which is consistent with expectations of more defects or atomic irregularities in association with smaller grain sizes (Cançado et al. 2011a). For increasing defect density for smaller grains, the 2*D* peaks also show significant broadenings of the full width at half-maximum (FWHM) (Eckmann et al. 2012).

2.4 *k* measurements of polycrystalline graphene

As earlier mentioned in Section 1.2.3, the thickness of graphene is too thin (~0.335 nm) to measure the thermal conductivity by the traditional technique, such as 3-ω method (Wang and Sen 2009). There are two representative methods to measure the thermal conductivity of graphene. One is micro-resistance thermometry (Seol et al. 2010; Jang et al. 2010; Pettes et al. 2011; Seol et al. 2011; Jang et al. 2013) and the other is optothermal Raman thermometry (Balandin et al. 2008; Cai et al. 2010; Chen et al. 2010; Faugeras et al. 2010; Chen et al. 2012b; Chen et al. 2012a).

The micro-resistance thermometry technique is a steady-state method to directly probe heat flows in materials with high resolution of temperature by employing electrical resistance as thermometers (Cahill et al. 2002). However, this technique needs many concomitant processes like too-complicated MEMS fabrication and the assumption of the contact resistance between graphene and substrate has large uncertainty.

The optothermal Raman thermometry technique is very simple method to measure the thermal conductivity of graphene without any complicated processes. When a laser light is focused at the center of graphene sheets, graphene temperature locally raises. The temperature increases by the absorbed laser power can be

measured using the relation between temperature and 2*D* peak position of graphene, because Raman 2*D* peak of graphene linearly shifts from 300 K to 500 K. Although the method has relatively large uncertainty, optothermal Raman technique is widely used for the thermal conductivity measurements of graphene due to its usability. Consequently, the thermal conductivity of graphene can be obtained by solving the heat transfer equation in which the measured temperature and optical absorption are used.

In this study, optothermal Raman technique is used to measure the thermal conductivity of prepared graphene samples. Therefore, how to measure the thermal conductivity of graphene samples will be discussed in this section. At first, the heat diffusion equation will be briefly presented in Section 2.4.1. The optical absorptions of graphene samples are measured by directly checking the transmittance using a power meter (Section 2.4.2). Then, the relation between 2D peak positions and graphene temperature will be discussed in Section 2.4.3 and the temperature rises as the absorbed laser power will be showed in Section 2.4.4. Finally, the measured thermal conductivities of graphene with different grain sizes will be presented in Section 2.4.5.

2.4.1 Heat diffusion equation

For the case of the suspended graphene ignoring the air convection losses

(Figure 2.12), obtaining the thermal conductivity of the suspended graphene is very simple. When the Raman laser beam of nominal radius r_0 is incident on the hole-suspended graphene of radius R and thickness t as depicted in Figure 2.13, the absorbed laser heating amount (aQ) is given by the incident laser power multiplied by the graphene absorption. Assuming negligibly small convection from the graphene surface to air (this assumption will be further assessed later in Section 2.5.3), the axisymmetric heat conduction equation determines the radial profiles of the temperature as a function of the in-plane thermal conductivity together with other known geometrical variables as follows

$$k_{sus} = \frac{aQ \ln\left(\dfrac{R}{r_0}\right)}{2\pi t (T_m - T_0)} \alpha \tag{2.1}$$

where the measured temperature at the laser spot area is determined from the $2D$ peak shift of Raman spectra. The Au/Cr contact layer temperature T_0 is set equal to the ambient temperature (this assumption will be validated later in Section 2.5.2) and $\alpha \sim 1.099$ represents an integral function of r_0 and R (Cai et al. 2010).

2.4.2 Optical absorption of graphene

The optical absorption of graphene should be measured to know the absorbed

power from Raman laser irradiation in optothermal Raman method. For the case of the suspended graphene on a through hole, the optical absorption of graphene can be measured directly by using power meter. Since graphene has negligible reflectance (<0.1 %) (Nair et al. 2008), the optical absorption of graphene can be easily measured by just checking the transmittance. Figure 2.14 shows the schematic illustration how to measure the optical absorption of suspended graphene on a through hole. At first, the power at a empty hole without hole P_{emty} is measured, then the transmitted power through graphene P_g is measured by power meter. Finally, the optical absorption of graphene is obtained from the difference between P_{empty} and P_g like Equation 2.2.

$$Optical\ absorption\,(\%) = \frac{P_{empty} - P_g}{P_{empty}} \times 100 \qquad (2.2)$$

The results of measured optical absorption of suspended graphene are summarized in Table 2.2. The optical absorptions of graphene samples are average values of 9~10 experiment data. For the tree samples with l_g = 4.1, 2.2, and 0.5 μm, the measured optical absorption ranges from 2.95 % to 3.17 %, showing no apparent correlation with the grain size but falls within the known range of absorption of single-layer CVD graphene (Chen et al. 2010; Chen et al. 2012a; Cai et al. 2010;

Chen et al. 2012b).

2.4.3 The correlation between 2*D* peak positions and temperature

In optothermal Raman technique, the temperature dependence of Raman peak shift should be known to measure the graphene temperature heated by Raman laser. In a previous study, Raman 2D peak down shifts with increasing stage temperature are larger than the Raman G peak down shifts (Chen et al. 2010). Therefore, in this study, 2*D* peak shifts are used to determine the graphene temperature in optothermal Raman method due to the higher temperature sensitivity. And very low power (below 0.05 mW) was used to avoid the local heating by the Raman laser illumination. In this step, Raman laser is not a heating source but a measurement instrument.

The temperature dependence of Raman 2*D* peak shift is facilitated from a calibration using a hot plate that provides an isothermal environment ranging from 300 K to 500 K in Figure 2.15, and thus any measured 2*D* peak shift can determine the graphene temperature from this calibrated correlation. The inset graph shows the total shift of the 2*D* peak of the suspended graphene with 4.1 μm average grain size when the hot plate temperature is increased from 300 K to 500 K. Linearly decreasing dependence like previous studies (Cai et al. 2010; Chen et al. 2010; Calizo et al. 2007) of Raman 2*D* peak shift with increasing hot plate temperature is

observed and provides the temperature coefficients $d\omega/dT$ = -0.0371, -0.0397, and -0.0597 cm^{-1}/K for the average grain sizes of 0.5, 2.2, and 4.1 μm, respectively.

2.4.4 The temperature rises as the absorbed laser power

To obtain the thermal conductivity of graphene with different grain sizes as temperature, the temperature rises were measured by controlling the absorbed laser power. Figure 2.16 shows the temperature rises with increasing the absorbed power from Raman laser illumination. The graph shows that for a fixed absorbed laser power, a larger increase in the measured temperature is measured for smaller grains. This means that the absorbed heat is less effectively conducted radially along the graphene, resulting in relatively higher measured temperature of graphene, and thus implying that the in-plane thermal conductivity of graphene with smaller grains is lower than that with larger grains.

2.4.5 Grain size dependent *k* of polycrystalline graphene

The thermal conductivities of suspended graphene with different grain sizes can be obtained by inserting experiment data into Equation 2.1. The measured in-plane thermal conductivities of graphene in Figure 2.17 show its grain size and temperature dependence for the range of average grain sizes from 500 nm to 10 μm. Each data point represents an average of 10 individual optothermal Raman

measurements. The single data point ($\diamondsuit$) represents the thermal conductivity of exfoliated graphene with supposedly infinite or very large grain size (Balandin et al. 2008). Considering the ballistic behavior of phonon inside grains and boundary scattering, the single-crystalline bulk graphene conductivities are estimated by extrapolation/fitting of the our experimental data as shown by the curve (the curve will be further discussed later in Section 2.5.4), which are comparable, within our experimental uncertainty ranges, with previous reports of both theoretical and experimental findings (Balandin et al. 2008; Ghosh et al. 2008a; Nika et al. 2011; Serov et al. 2013). The discrepancy of this measured k value from the ideal limit of calculations is possibly due to the edge effect associated with the relatively smaller dimension (3 μm) of the rectangular geometry of their suspended graphene on the trench of the same width. The high thermal conductivity of the graphene with the large grains of average size 10 μm can be attributed to the inclusive contributions from thermal conductance associated with the long-wavelength phonons (also with long λ_p) inside the grain as well as their relatively good transmittance across the grain boundaries. The air convection heat loss slightly overestimates the measured conductivity in air (the "×" symbols) than the measured conductivity in vacuum (the "+" symbols) as the heat loss is accounted for in the optothermal Raman process via enhanced thermal transport. For the graphene with smaller grain sizes of both 4.1 μm and 2.2 μm, the phonon dispersive range is reduced because of the

smaller sizes, which in turn limits the long-wavelength phonon contributions and ultimately results in lowered conductivities. When the grain size is further reduced to 500 nm, below the phonon mean-free path of graphene (~775 nm), a more substantial reduction of thermal conductivity is observed down to approximately 1/5 of that for 4.1 μm grains. In the case of supported graphene on a SiO_2 substrate, the non-equilibrium Green's function (NEGF) analysis also demonstrated that the in-plane thermal conductivity is subjected to a more distinctive decrease when the grain size approaches that of the phonon mean free path (Serov et al. 2013).

The thermal conductivity of graphene decreases with increasing temperature, attributing at least partially to the enhanced phonon-phonon Umklapp scattering at higher temperature (Cahill et al. 2014; Nika et al. 2009). This negative temperature dependence, however, gradually diminishes as the grain size decreases: $k \sim T^{-1.95}$, $T^{-1.38}$, $T^{-1.30}$, and $T^{-0.80}$ for l_g = 10, 4.1, 2.2, and 0.5 μm, respectively. (The power law for temperature dependence is obtained by fitting the measured average conductivities, and the coefficients of determination (R^2) are 0.953, 0.952, and 0.733, for grain sizes of 4.1, 2.2, and 0.5 μm, respectively.) Umklapp scattering and grain boundary scattering are regarded as two major scattering mechanisms of thermal carriers (i.e. phonons) in polycrystalline graphene. While the Umklapp scattering has strong temperature dependency due to increasing phonon populations at higher temperatures, grain boundary scattering depends on grain boundary

density or grain sizes in addition to temperature (Kaviany 2014). Theoretical analysis based on harmonic approximation demonstrates increasing boundary conductance with temperature as more phonons contribute to thermal transport (Pop et al. 2012). Therefore, the negative temperature dependence of thermal conductivity is weakened by increasing the boundary scattering dominance in smaller-grain polycrystalline graphene.

2.5 Analysis of experimental results

In this section, various heat transfers will be assessed by numerically solving heat diffusion equations. At first, uncertainty of the measured thermal conductivities will be estimated by root-sum-square method (Moffat 1988) in Section 2.5.1. Then, hole edge temperature of suspended graphene with different grain sizes will be calculated to validate the assumption that the hole edge temperature is equal to the ambient temperature used in Equation 2.1 and the effect of air convection losses will be examined by solving the full energy balance equation in Section 2.5.2 and 2.5.3, respectively. Also, the thermal conductivity of the single-crystalline graphene without grain boundaries will be obtained by fitting to the simple linear chain model of polycrystalline thermal transport (Shin and Kaviany 2011; Yang et al. 2002) in Section 2.5.4. Finally, local nonequilibrium (NE)

between different phonon polarizations (Vallabhaneni et al. 2016; Sullivan et al. 2017) will be confirmed by comparing the measured temperature from Raman $2D$ peak shifts and Raman G peak shifts in Section 2.5.5.

2.5.1 Uncertainty of k measurements

The uncertainty of the measured thermal conductivity is estimated by the so-called "root-sum-square" method (Moffat 1988) as given by:

$$U_k = \sqrt{\left(\frac{\partial k}{\partial Q}\right)^2 \left(U_Q\right)^2 + \left(\frac{\partial k}{\partial \Delta T}\right)^2 \left(U_{\Delta T}\right)^2} \qquad (2.3)$$

Where the weighting values of $\dfrac{\partial k}{\partial Q}$ and $\dfrac{\partial k}{\partial \Delta T}$ are determined from Equation 2.3. Both elementary uncertainties of U_Q and $U_{\Delta T}$ can be given by $t_{0.025}(n-1)\dfrac{s}{\sqrt{n}}$, where s represents the sample standard deviation, n is the number of experimental data realizations ($n = 10$ for most of our experiments), and $t_{0.025}(n-1)$ is the standardized random variable of Student's t distribution at the 95% confidence level. The resulting overall uncertainties U_k are shown as error bars in Figure 2.17. The relative uncertainties U_k/k ran

ge about ±22 % for graphene samples with 4.1 mm grains for all the teste
d temperatures, range from ±16 % to ±24 % for 2.2 mm grains, and range
from ±15 % to ±28 % for 0.5 mm grains. All uncertainties of the measured
thermal conductivities of graphene with grain sizes of 0.5, 2.2, and 4.1 μ
m are summarized in Table 2.3.

2.5.2 Hole edge temperature of suspended graphene

When obtaining the thermal conductivity of suspended graphene by using
Equation 2.1, the hole edge temperature is assumed to be the ambient temperature.
In order to validate the assumption of ambient temperature at the hole-edge, we
have conducted an analytical examination to delineate the potential heat losses to
the substrate as well as to the contacting air environment. Considering the
suspended graphene on a hole of radius $R = 4$ μm and then supported thereafter for
$r > R$ (Figure 3.3), the heat transfer governing equations are given by:

$$k_{sus}t\frac{1}{r}\frac{d}{dr}\left(r\frac{dT}{dr}\right)-2h(T-T_a)+q''(r)=0 \text{ for } r < R \qquad (2.4)$$

$$k_{sup}t\frac{1}{r}\frac{d}{dr}\left(r\frac{dT}{dr}\right)-g(T-T_a)+q''(r)=0 \text{ for } r > R \qquad (2.5)$$

where h is the convection heat transfer from graphene to air ($h = 2.9$ x 10^4 W/m^{2}K,

as experimentally driven by Chen et al, ACS Nano, 2011, 5(1), pp321-328), g is the total interface thermal conductance per unit area between graphene and the Au/silicon nitride substrate (g = 2.8 x 10^7 W/m^{2}K provided by Cai et al, Nano Letters, 2010 10(5), pp1645), $q''(r)$ is the Gaussian distribution of incident laser energy flux, k_{sus} represents the thermal conductivity of the suspended portion of graphene (unknown; to be determined), and k_{sup} represents the thermal conductivity of the supported portion of graphene (k_{sup} = 370 W/m·K given for a similar configuration at 300K by Weiwei Cai et al., 2010). These two equations are simultaneously solved by the Gauss-Seidal method with two boundary conditions, $dT/dr = 0$ at $r = 0$ and the ambient boundary condition of $T = T_a$ at a sufficiently large radial distance, namely $r = 20$ µm.

Numerical solutions of the full heat transfer governing equations, accounting for the possible heat losses along the supported graphene as well as through the substrate - so-called parasitic thermal resistors, show that the discrepancy between the calculated hole-edge temperature and the ambient temperature T_a is less than 1 K for the all tested cases as summarized in Table 2.4. This validates the aforementioned assumption in that the hole-edge temperature is equal to the ambient temperature T_a within 0.34% accuracy and that the heat leakage through the supported graphene/substrate is negligibly small. Furthermore, the corresponding errors in thermal conductivity due to the edge temperature

discrepancies (maximum 0.34%) spans to 0.41%, and these error bounds are substantially narrower than the thermal conductivity-measurement uncertainty, which ranges from ±15% up to ±28%.

2.5.3 The effect of air convection losses

Despite the earlier finding of a minor correction requirement for the air convection loss for the case of graphene sample with relatively large 10-μm grain size (Chen et al. 2010), the air convection loss effect on thermal conductivity is re-examined for the graphene samples with the present smaller grain sizes. In lieu of using Equation 2.1, the full energy balance equation (Equation 2.4) that governs the heat transfer of the suspended graphene under the air convection loss was numerically solved, using the previously estimated air convection coefficient of $h = 2.9 + 5.1/-2.9 \times 10^4$ W/m^2·K (Chen et al. 2010). In attempts to determine thermal conductivity, accounting for the air convection loss, the main obstacle was estimating the unknown convection coefficient h. To our best knowledge, the only published estimation of h is available from Chen et al.'s experimental comparison of thermal conductivity measured once in a vacuum and once in an air environment (ACS Nano, 2011, 5(1), pp. 321-328). They performed the experiment for CVD graphene with unknown grain size and presented $h = 2.9 + 5.1/-2.9 \times 10^4$ W/m^{2}K with excessively large uncertainties, i.e., the estimated h ranged from 0 to 8.0×10^4

W/m^{2}K at a given constant temperature of 510 K. Note that additional uncertainties can be imposed upon h when applied to different grain samples with different grain sizes, test temperatures lower than 510 K, and inevitable defects and residues resulting from the transfer process. Nevertheless, we have used their mean value of $h = 2.9 \times 10^4$ W/m^{2}K to numerically solve Equation 2.4.

For the two grain sizes of 4.1 and 2.2 μm, the discrepancies associated with the convection heat loss span up to 20% (Figure 2.18), which are fairly within the thermal conductivity measurement uncertainty ranges (±16 % ~ ±24 %). For the graphene samples with the smallest 0.5 μm grains (Figure 2.18), the relative deviations appear greater due to the substantially lowered thermal conductivity, while the deviation magnitudes are actually smaller compared with the previous two cases with bigger grains. Additionally, these thermal conductivity discrepancies may be exaggerated due to the excessively large uncertainties of the available h value, which presents a wide range from 0 to 8.0×10^4 W/m^2·K (Chen et al. 2010). Despite these uncertainties, the convection air loss effect turns out to be nontrivial for smaller grain size cases. However, since our study is focused on the lowered thermal conductivity due to the reduced grain sizes and its relative comparison, the degree of persistent overestimation of thermal conductivity when neglecting the air convection loss does not substantially affect the main discussions.

On the other hand, the radiative heat losses turned out to be quite negligible for

all tested cases. The radiation heat transfer coefficient is given by

$h_{rad} = \varepsilon\sigma(T + T_a)(T^2 + T_a^2)$, where σ is the Stefan-Boltzmann constant (5.670×10^{-8}

$\text{W·m}^{-2}\text{·K}^{-4}$) and the emissivity $\varepsilon = 1.0$, assuming a blackbody emission. For the

upper limit temperature of 550 K, the maximum h_{rad} is estimated to be 18.92

$\text{W/m}^2\text{K}$, which is quite negligible compared with the estimated convection heat

transfer coefficient $h = 2.9 \times 10^4 \text{ W/m}^2\text{K}$.

2.5.4 Thermal conductivity of the single-crystal graphene

The simple linear chain model of polycrystalline thermal transport (Shin and Kaviany 2011; Yang et al. 2002) depicts the overall thermal resistance of polycrystalline graphene, RE_{PG}, as the sum of contributions from the resistance of the grain interior, RE_G, and the resistance associated with the grain boundaries, RE_{GB} (Wu et al. 2014); i.e., $RE_{PG} = RE_g + RE_{GB}$. Here, $RE_{GB} = 1/G_{GB}$, the inverse of grain boundary conductance G_{gb}, $RE_{PG} = l_g/k_{PG}$, where l_g represents the grain size, and k_{PG} is the effective conductivity of polycrystalline graphene, and similarly, $RE_g = l_g/k_g$. Thus we have:

$$\frac{1}{k_{PG}} = \frac{1}{k_g} + \frac{1}{l_g G_{GB}} \tag{2.6}$$

where k_g is also grain-size dependent unless l_g is much longer than the phonon mean free path, i.e., $l_g \gg \lambda_p$, only for the case of dominating diffusive regime with minimum ballistic effect. Note that the edge effect of the suspending hole is excluded herein due to the sufficiently large hole with $Kn > 5$.

If l_g is much shorter than the mean free path, i.e., $l_g \ll \lambda_p$, the resulting thermal transport is predominantly governed by the ballistic (scattering-free) conductance G_{Ball}.(Mingo and Broido 2005; Munoz et al. 2010) The ballistic thermal conductivity of the grain interior region is thus given by $k_g \sim k_{Ball} = G_{Ball}l_g$, and here G_{ball} is calculated from the Landauer formula associated with the phonon dispersion relation $\omega_p = \omega_p(\kappa_p, j)$, where ω_p is phonon angular frequency, κ_p is wavevector, and j is phonon mode (Munoz et al. 2010; Rego and Kirczenow 1998):

When the grain sizes are comparable to the phonon mean free path ($l_g \sim \lambda_p$), k_g is approximated by a Landauer-like approach (Prasher 2008; Pop et al. 2012; Bae et al. 2013) (including angle averaging in 2D for the backscattering length) as follows:

$$k_g = G_{Ball} \left(\frac{1}{l_g} + \frac{2}{\pi \lambda_p} \right)^{-1} \qquad (2.7)$$

For the present test range of l_G, combining Equation 2.6 and 2.7 gives the

polycrystalline graphene conductivity:

$$\frac{1}{k_{PG}} = \left(\frac{1}{G_{Ball}} + \frac{1}{G_{GB}} \right) \frac{1}{l_g} + \frac{2}{\pi G_{Ball} \lambda_p} \qquad (2.8)$$

i.e., with l_g-independent G_{Ball} and G_{GB}., $1/k_{PG}$ is given as a linear function of $(1/l_g)$. Using the power-law fitting ($T^{-1.38}$, $T^{-1.30}$, and $T^{-0.80}$), k_{PG}'s with three l_g's (4.1, 2.2 and 0.5 µm) are calculated with respect to T. The least squares fitting of Equation 2.8 for the k_{PG} data with the three l_g's predicts the grain size dependence of the polycrystalline graphene conductivity as shown in Figure 2.19a. Here, the fitting parameters are G_{GB} and λ_p, whereas G_{Ball} is given by theoretical calculations (Mingo and Broido 2005; Munoz et al. 2010).

The single-crystalline bulk graphene conductivity k_{SG} is calculated as $l_g \rightarrow \infty$ in the fitting equation; for example, $k_{SG} = 6508$, 3272, and 2062 W/m-K for the three selected temperatures of 300, 400, and 500 K, respectively. From either Equation 2.7 or Equation 2.8, k_{SG} is also expressed as $\pi G_{Ball} l_p / 2$. Using the G_{Ball} from Bae et al. (Bae et al. 2013) with the k_{SG} calculated from the linear fitting, the effective phonon mean free path λ_p is estimated to be 979.9, 361.7, and 188.8 nm, respectively for the three temperatures. Note that since λ_p is a function of phonon mode and wavevector, the calculated λ_p is the effective mean free path, which is averaged over the ranges of the mode and wavevector. Due to a wide distribution

of the phonon mean free path (higher frequency or energy, longer mean free path) (Feng et al. 2015; Singh et al. 2011), i.e., length dependence, different phonon contributions to thermal transport are expected depending on the grain size. Although these experimentally fitted λ_p and k_{SG} correspond reasonably well with previous reports of both theoretical and experimental findings (Balandin et al. 2008; Ghosh et al. 2008a; Nika et al. 2011), these can be regarded to be slightly overestimated, because low-frequency phonons have higher transmission across grain boundaries and can influence overall thermal transport (Serov et al. 2013).

Complete temperature dependence curves for both k_{SG} and λ_p are shown in Figure 2.19b. As expected through the kinetic theory $k \sim cv\lambda$ (where c is heat capacity, v is phonon velocity, and λ is the mean free path (Jeong et al. 2011)), shorter λ_p for higher T due to the enhanced phonon-phonon scattering leads to lower k_{SG}. As phonon heat capacity c_p increases persistently with T in graphene (nearly doubled from 300 K to 600 K(Tohei et al. 2006; Nihira and Iwata 2003)) with very high Debye temperature $T_D \sim 2100$ K (Tohei et al. 2006; Tewary and Yang 2009), the decrease rate of k_{SG} is smaller than λ_p. Here, k_{SG} provides the upper limit of k_{PG}, and λ_p represents the grain size dependence of k_g (the longer λ_p, the larger l_g-dependence of k_g). Thus, polycrystalline graphene conductivity at higher T (shorter λ_p) is lower and increases more slowly with increasing l_g as previously shown in Figure 2.19a.

2.5.5 Temperature discrepancies by nonequilibrium of phonons

Due to a large relaxation time mismatch between different energy carriers and tightly focused laser spots smaller than the thermalization length, local NE between different phonon polarizations is expected inside the laser spot (Vallabhaneni et al. 2016; Sullivan et al. 2017). While the most prominent 2D peak shifts were used in determining our temperature data T_{2D}, the next prominent G peak shifts have now been additionally examined to assess any discrepancies between T_G and T_{2D} in Table 2.5. The slightly higher T_G compared with T_{2D} for the tested laser power range of 3.5 to 4.5 mW shows that the phonon system is not fully thermalized to an equilibrium. This can be attributed to the fact that population of high energy LA and TA phonons influences Raman G peak shift, while Raman 2D peak shift is affected by near Brillouin zone center phonons with lower energies (Bonini et al. 2007). The temperature discrepancies between T_G and T_{2D}, ranging from 2.63 % to 8.47 % for the tested laser power range, are within the relatively large Raman measurement uncertainties ranging from ±15 % up to ±28 %. This supports that the NE effect possibly increases the overall measurement uncertainties, however, we believe that this does not contradict our main findings of the grain size effects on thermal conductivity of graphene.

2.5 Conclusion

In order to observe grain boundary effects on thermal transport in polycrystalline graphene grown by CVD, 3 graphene samples with different grain sizes were synthesized by controlling synthesis conditions, such as operating pressure, temperature, heating/cooling time intervals and precursor gas concentration ratios ($CH_4:H_2$). And the polycrystalline graphene with different grain sizes were suspended on a thorough 8-μm hole to investigate only grain boundary effect on thermal conductivity except for the substrate contributions.

Then, the surface condition of all samples were visually confirmed by optical microscopy and SEM. Finally, the number of layer, quality, and defect density of all samples were characterized by Raman spectroscopy. And the average grain sizes of polycrystalline graphene were defined by MDA and digital image processing as 0.5, 2.2, and 4.1 μm. As a result, it was confirmed that graphene samples for thermal conductivity measurements are successfully prepared.

In this thesis, thermal conductivity of graphene was measured by using temperature-dependent Raman $2D$ peak shifts that is called optothermal Raman method. As a results, the measured thermal conductivities for 320 K $< T <$ 510 K are measured to be 2660-1230, 1890-1020, and 680-340 W/mK for average grain sizes of 4.1, 2.2, and 0.5 μm, respectively. Thus, significant reduction of thermal

conductivity is achieved when the grain size is decreased from 4.1 μm down to 0.5 μm, due to enhanced grain boundary scattering.

Furthermore, the experimental results are elaborated. First of all, uncertainties of the measured thermal conductivities are estimated by root-sum-square method and uncertainties of suspended graphene with different grain sizes range from ±15 % up to ±28 %. Uncertainties of supported HG with different porosities (about ±17 %) are slightly lower than that of suspended graphene, because of ultra-thin substrate that minimize the heat dissipation into substrate. However, HG with 4.91 % porosity shows relatively high uncertainty due to low Raman $2D$ peak intensity which allows low resolution in curve fitting to find the center of Raman $2D$ peak.

The temperature of suspended graphene at the hole edge was calculated by numerically solving full energy balance. As the result, the discrepancies between the calculated temperature of suspended graphene at hole edge and ambient temperature (~300 K) were too small (below 1 K). The re-obtained thermal conductivity considering the calculated hole edge temperature of suspended graphene shows 0.5 % error compared with the thermal conductivity when using the boundary condition that the hole edge temperature of suspended graphene is equal to ambient temperature.

The thermal conductivities considering the effect of air convection loss were lower than those no considering the effect of air convection loss about all graphene

samples. However, the differences fall within the error bar of measured thermal conductivities. Therefore, it is reasonable to analyze thermal transport in graphene using the measured thermal conductivities no considering the effect of air convection loss, because the used convection heat transfer coefficient has very large uncertainty.

The NE effect was confirmed by comparing the discrepancies between temperature from G peak and $2D$ peak shifts. There are some temperature discrepancies between T_G and T_{2D} ranging from 2.63 % to 8.47 % for the tested laser power range. It is clear that the small heat size (laser beam diameter) cause the nonequilibrium phonons, however, the error has no critical effect on main findings of the grain size effects on thermal conductivity of graphene.

The thermal conductivities of single-crystal graphene as temperature were anticipated by a simple chain model based on the experimental data, and it was shown a good trend with the measured thermal conductivities of suspended graphene with different grain sizes.
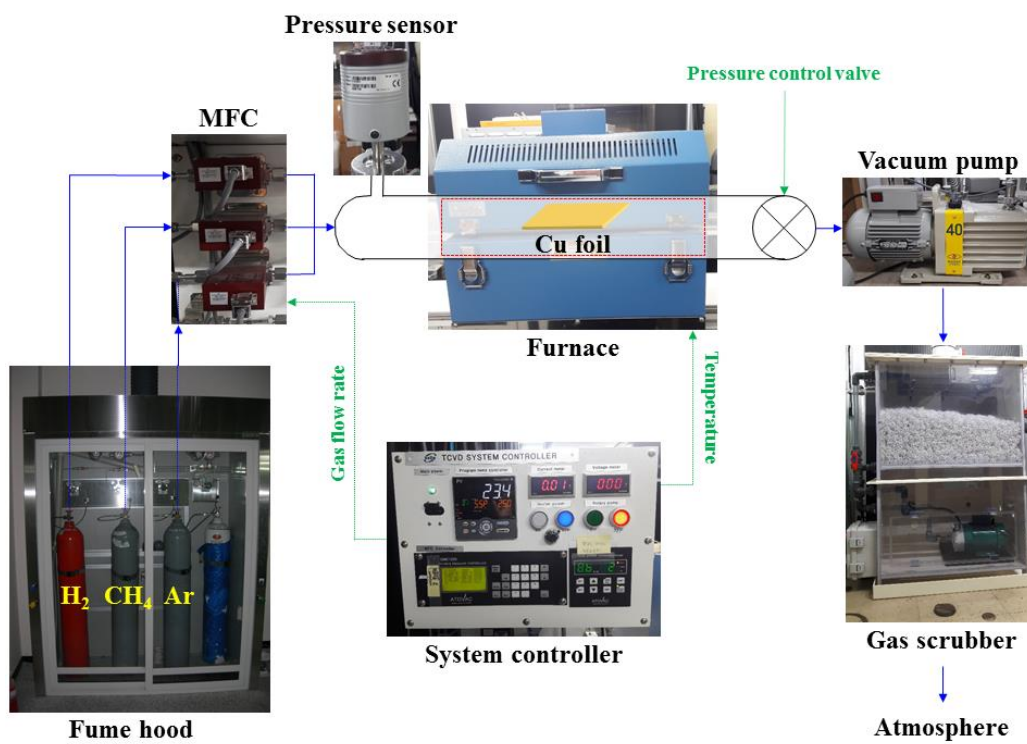
Figure 2.1 Experimental setup of CVD system

Table 2.1 CVD operation matrix for polycrystalline graphene synthesis with different grain sizes

Average grain sizes (μm)	0.5	2.2		4.1	
CVD synthesis temperature (℃)	800	900		4.1	
CVD synthesis pressure (Torr)	1.09	Step 1	Step 2	Step 1	Step 2
		0.37	1.08	0.19	0.30
Cursor gas volume flow rate ratio for CH$_4$:H$_2$	200:100	80:5	200:100	30:5	60:5
Cursor gas flow duration (min)	25	20	10	10	5
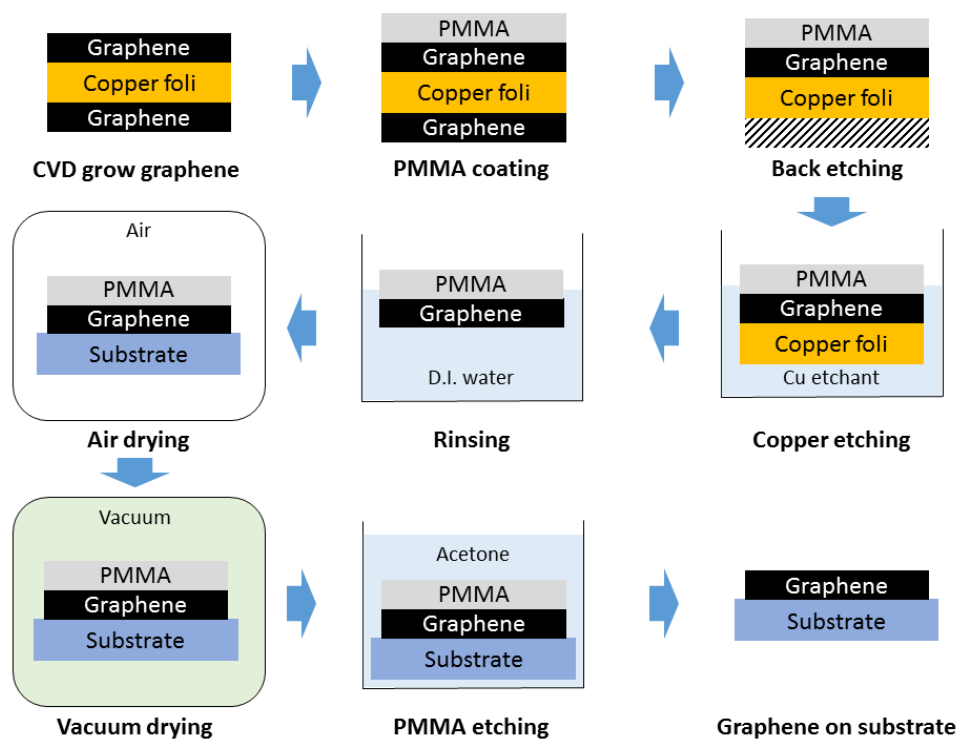
Figure 2.2 The process of transfer to the target substrate via PMMA
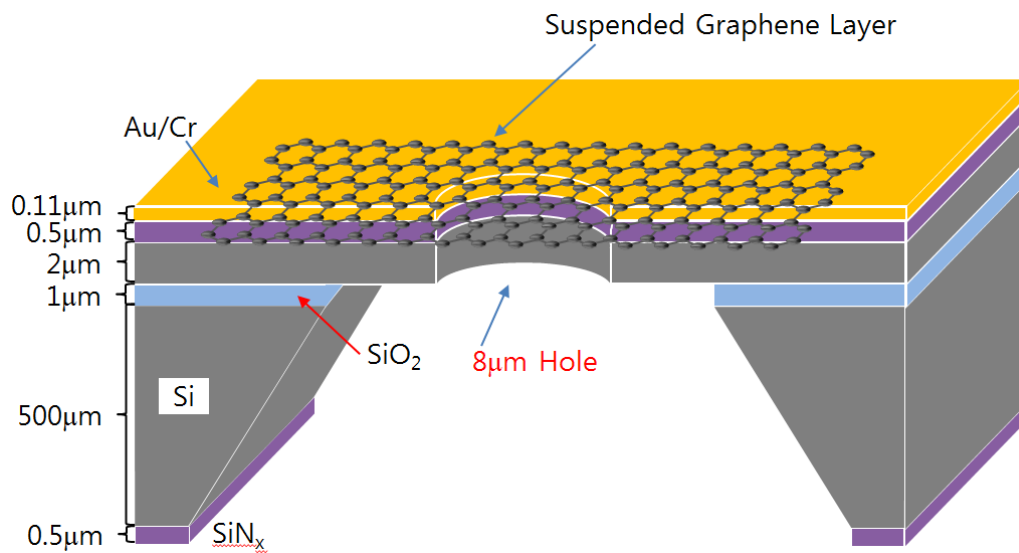
Figure 2.3 Schematic of suspended graphene on the hole pattern that was made by MEMS process including the DRIE and wet etching of a silicon-nitride (Si_3N_4) substrate
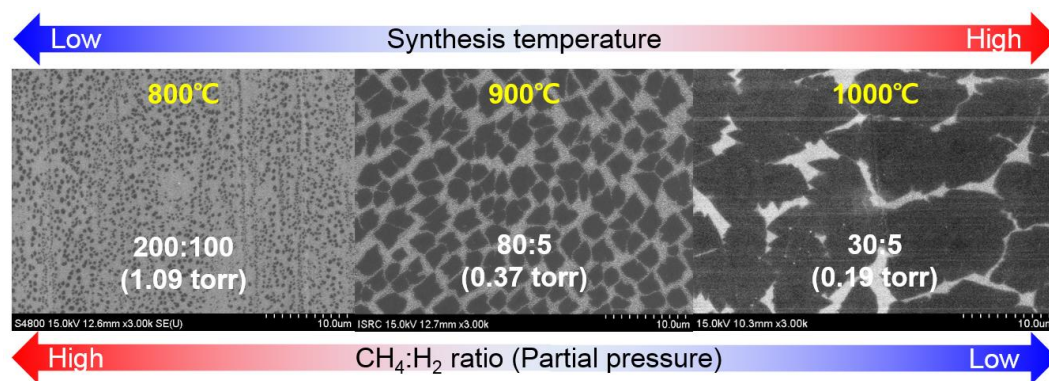
Figure 2.4 SEM images of different nucleation densities in the initial growth state depending on the synthesis temperature pressure
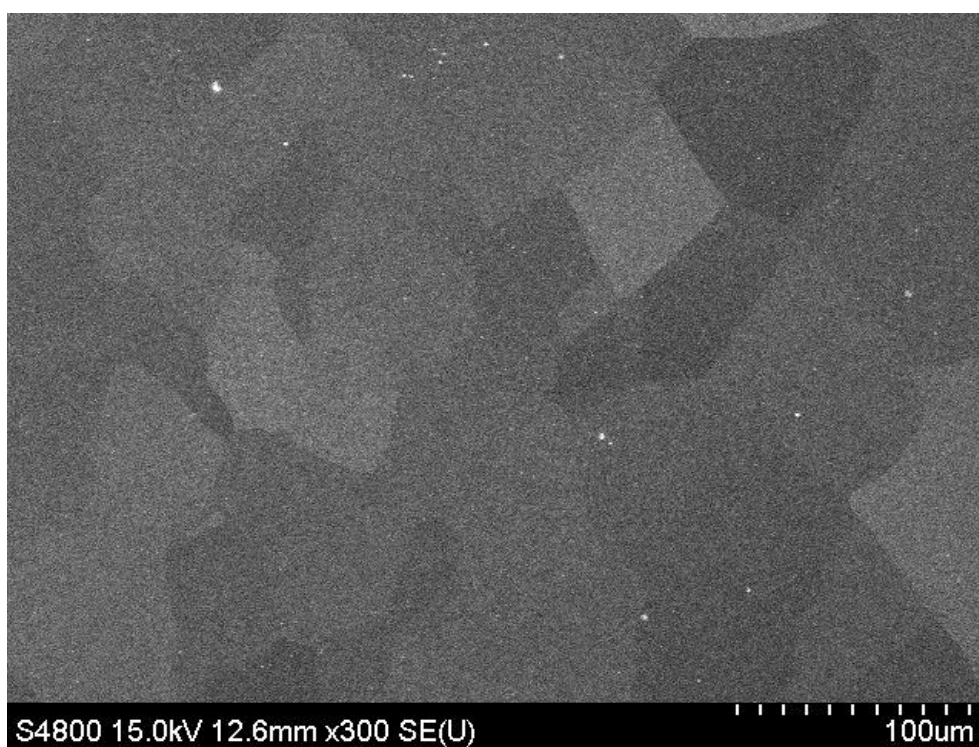
Figure 2.5 SEM image of the fully-grown CVD graphene
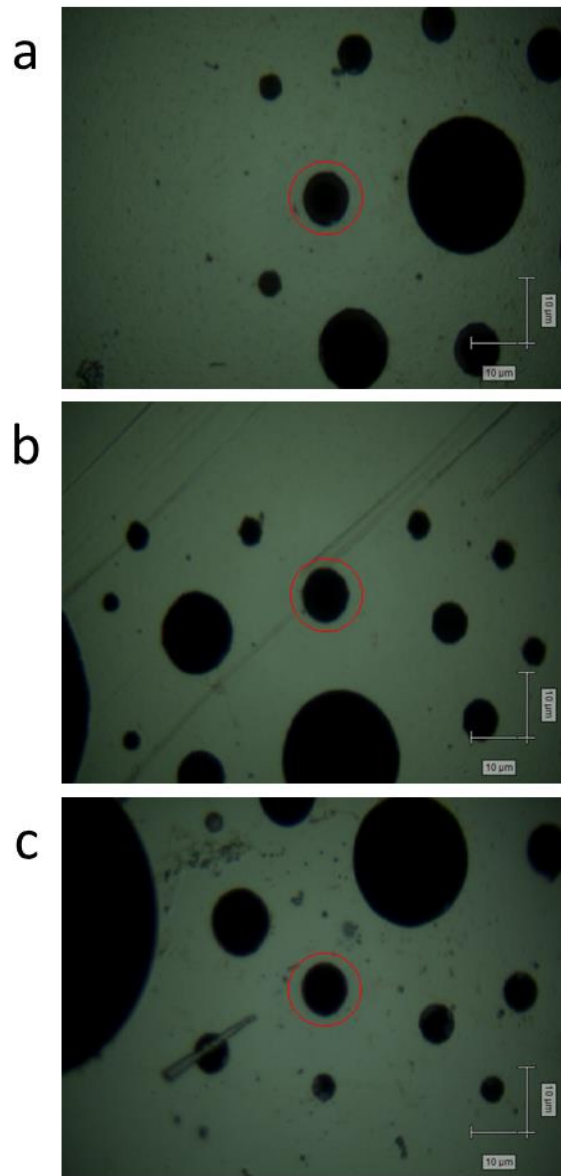
Figure 2.6 Optical images of the suspended graphene with grain sizes of (a) 4.1, (b) 2.2, and (c) 0.5 μm
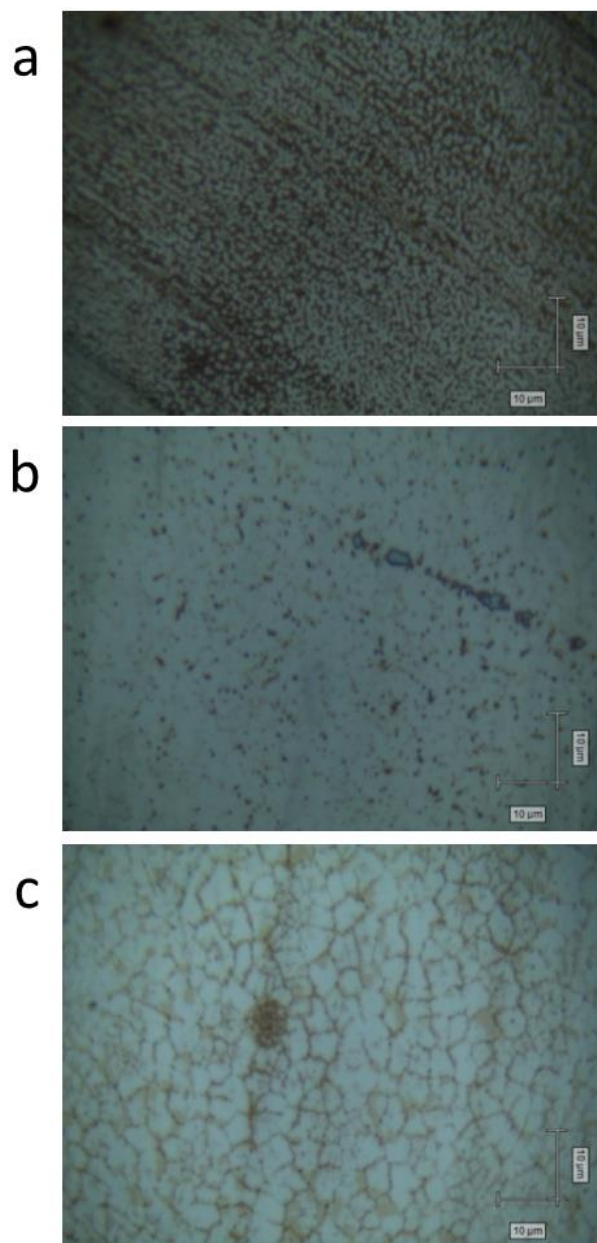
Figure 2.7 Optical images of graphene samples with grain sizes of (a) 0.5, (b) 2.2, and (c) 4.1 μm after MDA treatment
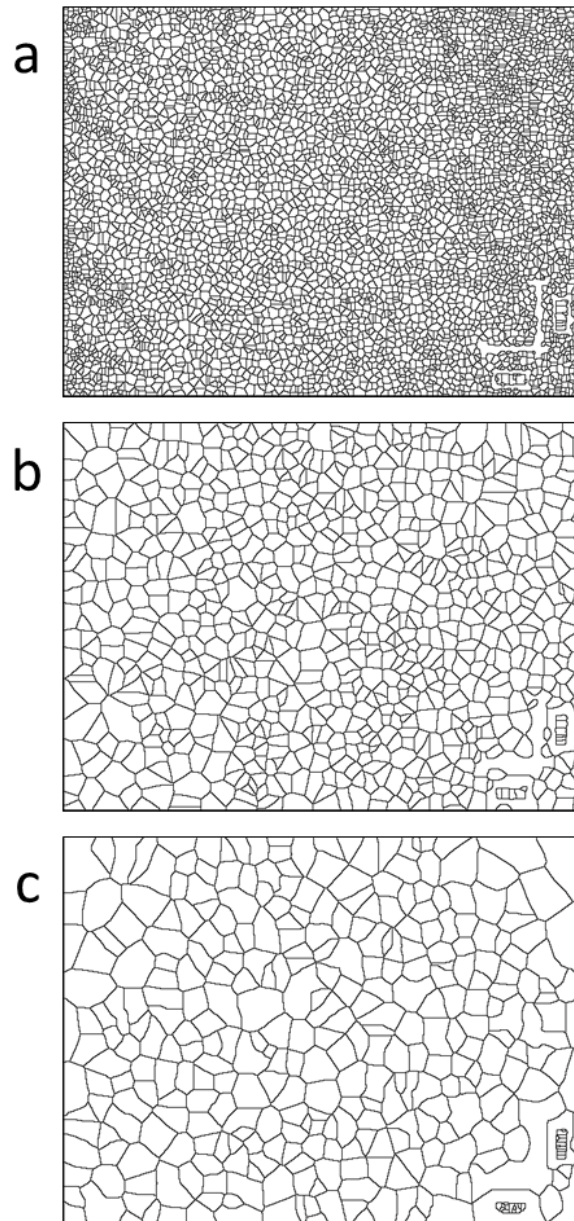
Figure 2.8 The images of clear grain boundaries of graphene with grain sizes of (a) 0.5, (b) 2.2, and (c) 4.1 μm after digital image processing
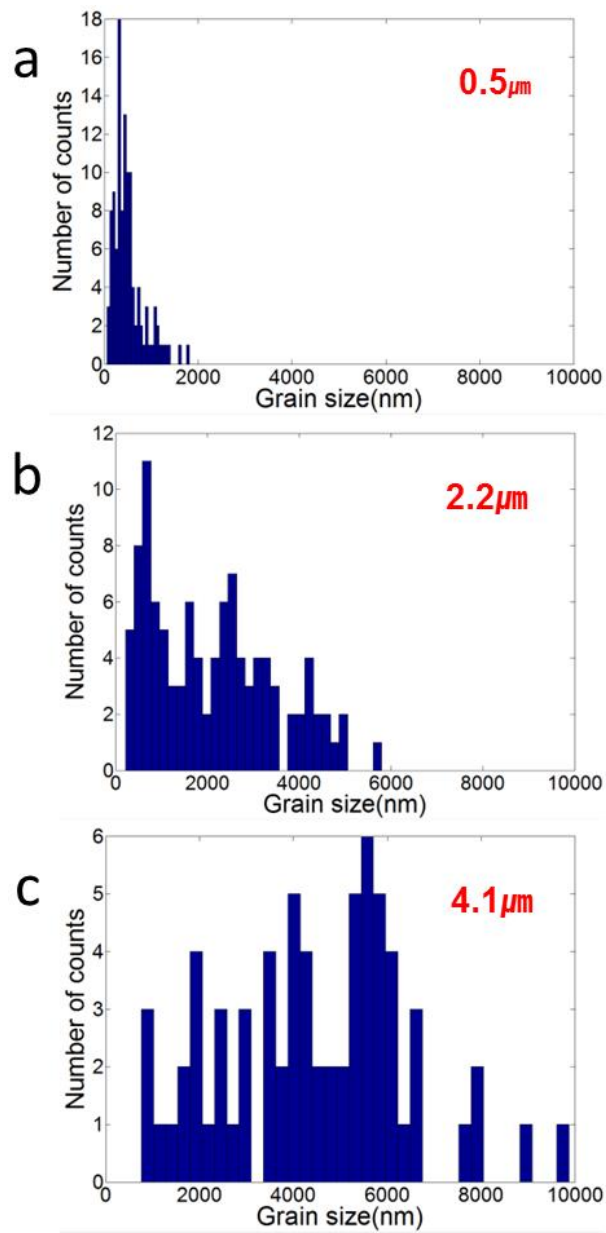
Figure 2.9 The distribution histograms of grain sizes about (a) 0.5, (b) 2.2, and (c) 4.1 μm
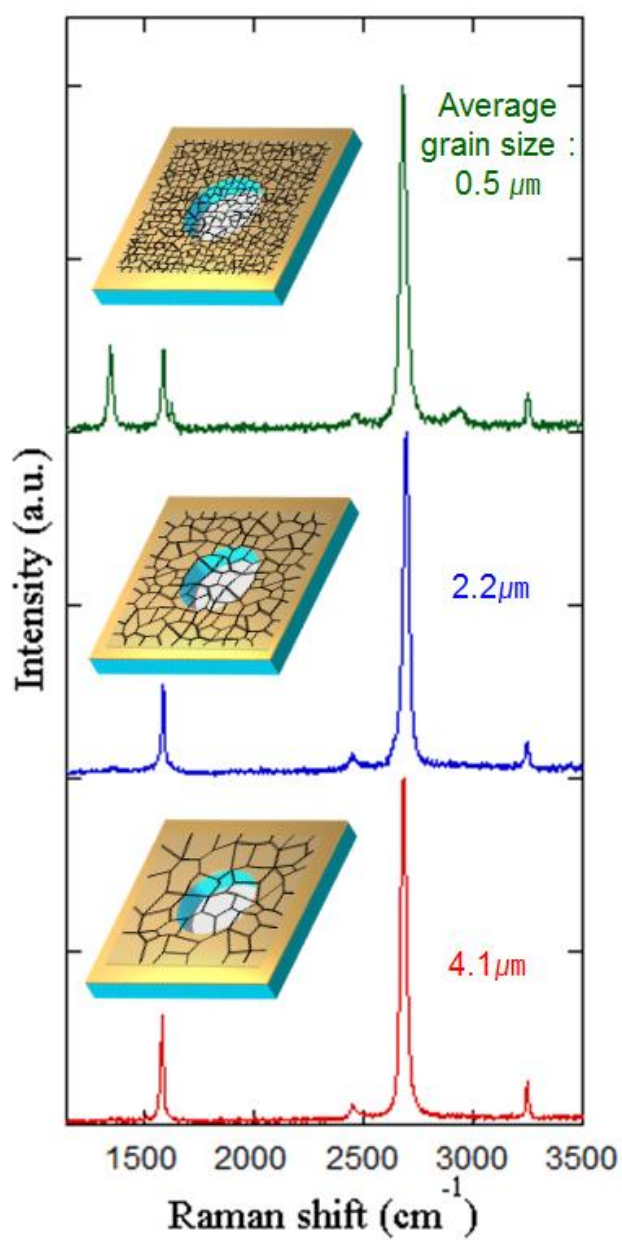
Figure 2.10 Raman spectra of graphene sheets with different grain sizes suspended on the 8 μm hole
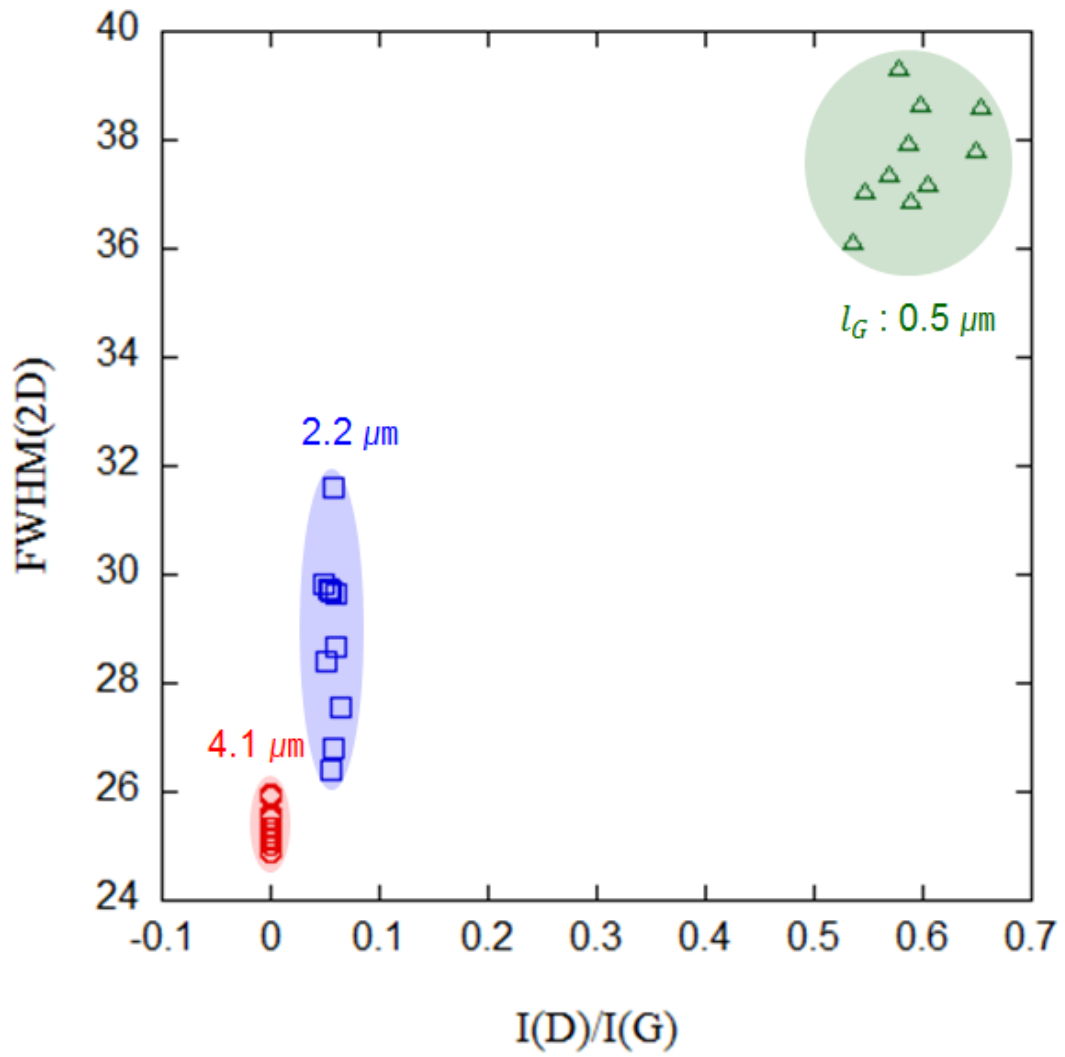
Figure 2.11 The ratio of Raman D peak to G peak versus the FWHM of 2D peak. These multiple data points were measured at random area in the same samples for each grain size
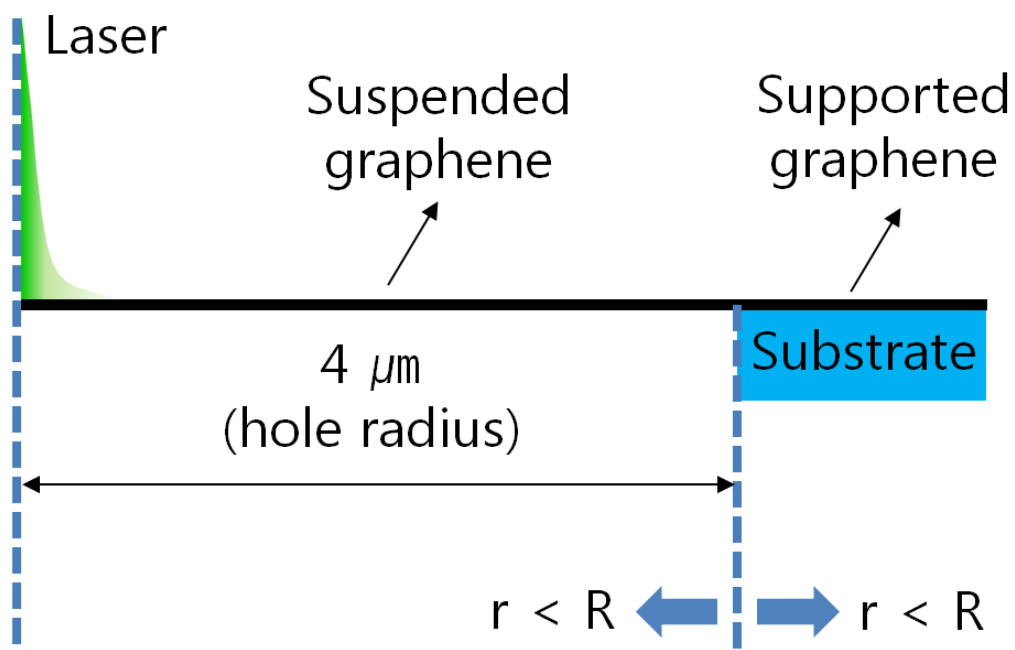
Figure 2.12 Schematic illustration of the suspended graphene on a hole of radius
R = 4 μm and supported thereafter
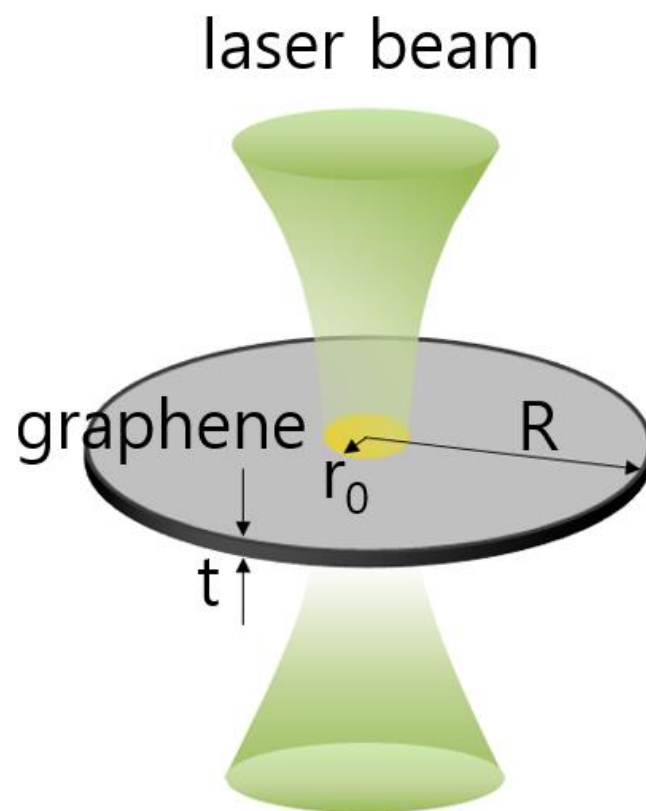
Figure 2.13 Schematic illustration of Raman laser beam of nominal radius on the hole-suspended graphene
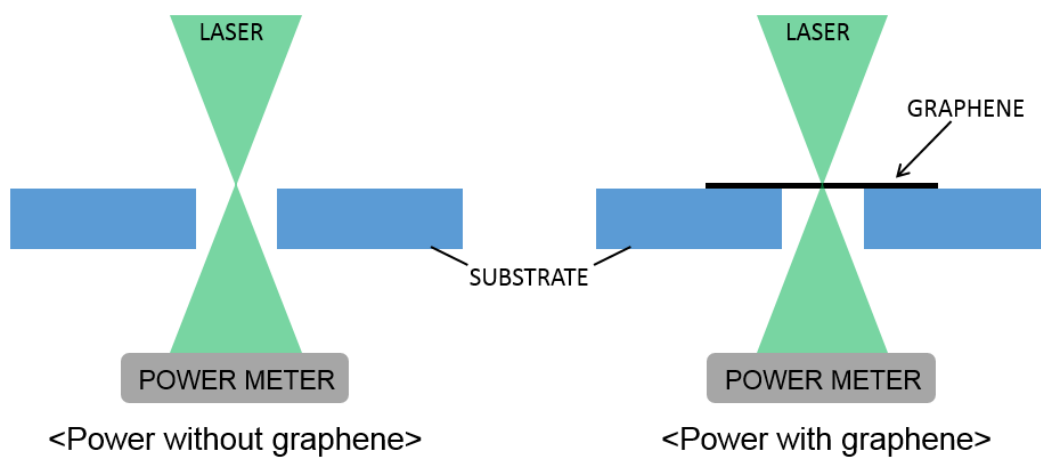
Figure 2.14 Schematic illustration how to measure the optical absorption of the suspended graphene on a through hole

Table 2.2 Summary of raw data about the measured optical absorption of graphene with grain sizes of 4.1, 2.2, and 0.5 μm

Grain size : 4.1 μm			Grain size : 2.2 μm			Grain size : 0.5 μm		
P_{empty}	P_g	a	P_{empty}	P_g	a	P_{empty}	P_g	a
[mW]	[mW]	[%]	[mW]	[mW]	[%]	[mW]	[mW]	[%]
3.13	3	4.15	2.74	2.65	3.28	0.513	0.495	3.50
3.54	3.38	4.51	1.378	1.332	3.33	0.513	0.496	3.31
3.54	3.44	2.82	1.378	1.349	2.10	0.513	0.499	2.72
4.36	4.25	2.52	1.042	1.02	2.11	0.507	0.489	3.55
4.34	4.2	3.22	1.047	1.003	4.20	0.508	0.505	2.50
4.34	4.22	2.76	2.90	2.80	3.44	0.494	0.477	3.44
4.33	4.22	2.54	2.88	2.79	3.12	0.506	0.494	2.37
4.33	4.22	2.54	2.88	2.79	3.12	2.804	2.731	2.60
4.33	4.23	2.30	2.89	2.79	3.46	2.782	2.712	2.51
4.02	3.9	2.98	2.89	2.8	3.11	average		2.95
average		3.17	average		3.13			
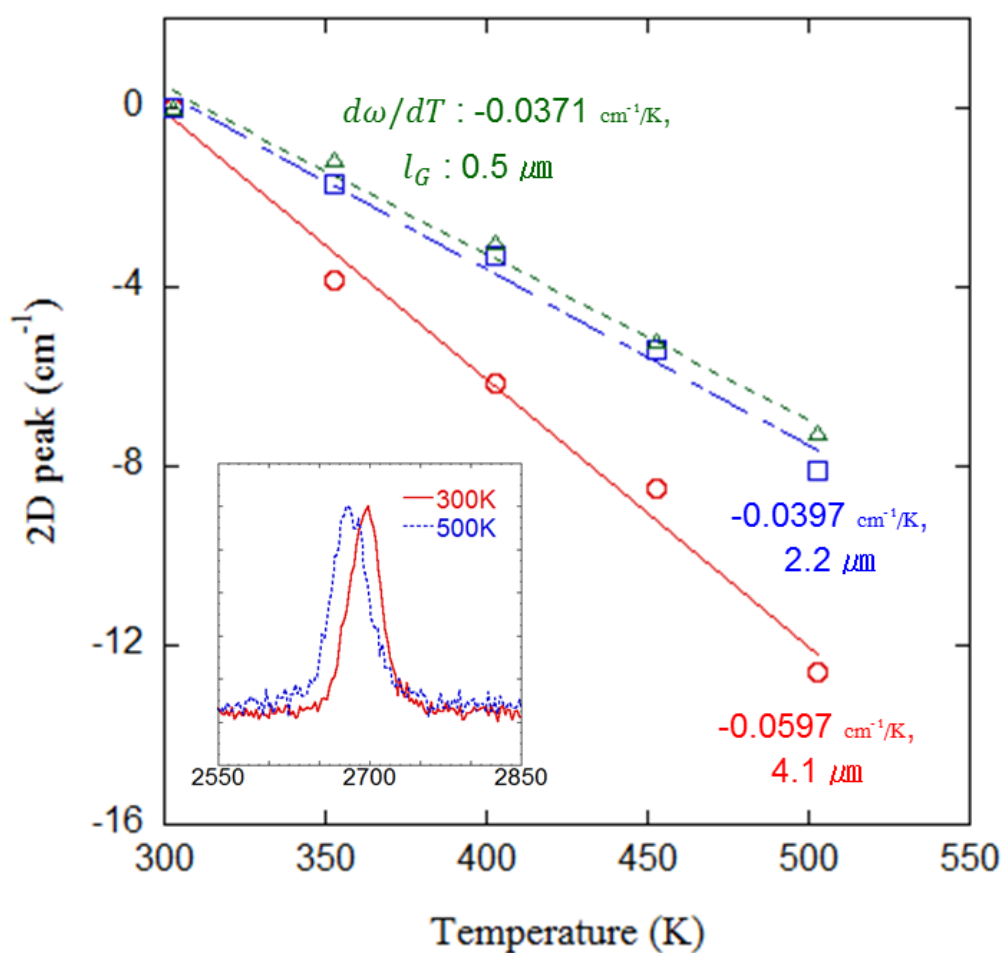
Figure 2.15 The correlation between the 2*D* peak positions and the temperature of graphene with grain sizes of 0.5, 2.2, and 4.1 μm. The inset shows the 2*D* peak shifts of the suspended graphene with 4.1 μm average grain size corresponding to the temperature change from 300 K to 500 K
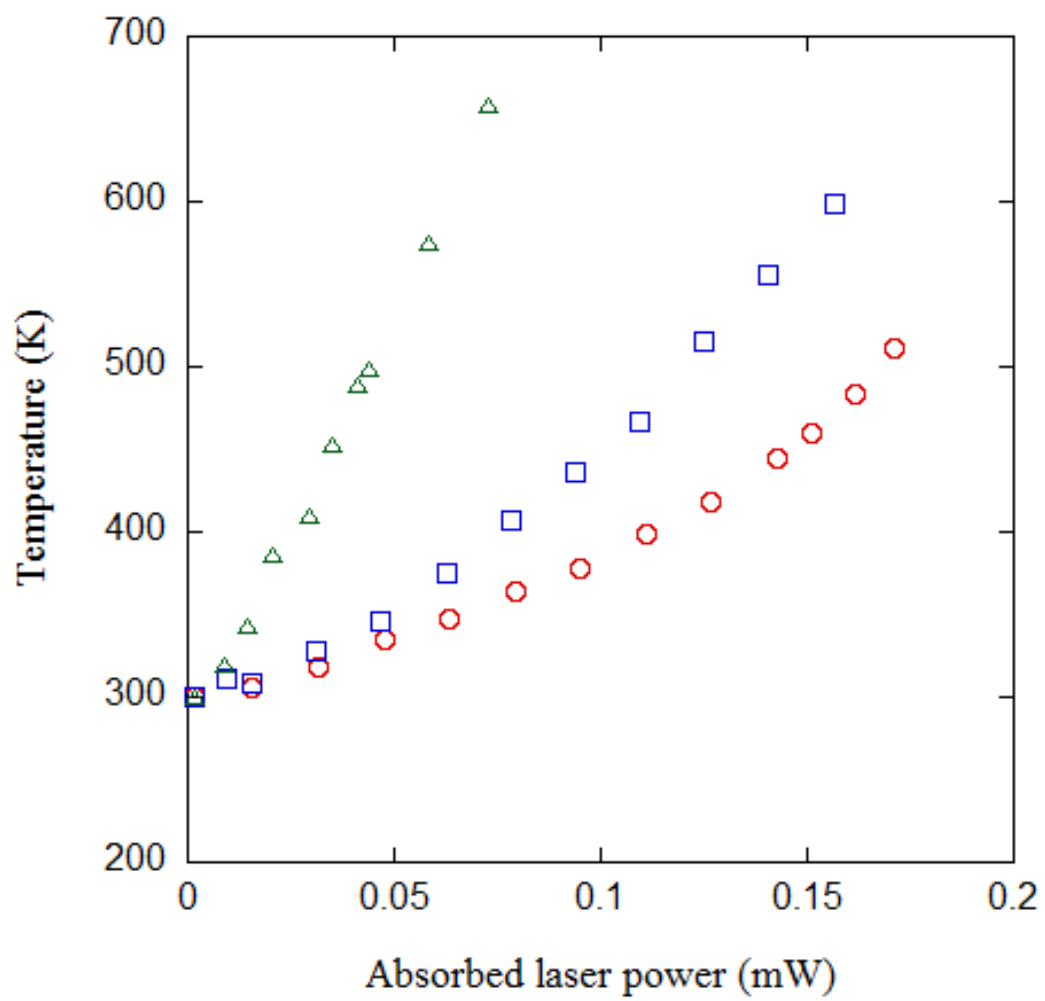
Figure 2.16 The measured temperature rises as the absorbed laser power increases for each graphene with grain sizes of 0.5, 2.2, and 4.1 μm
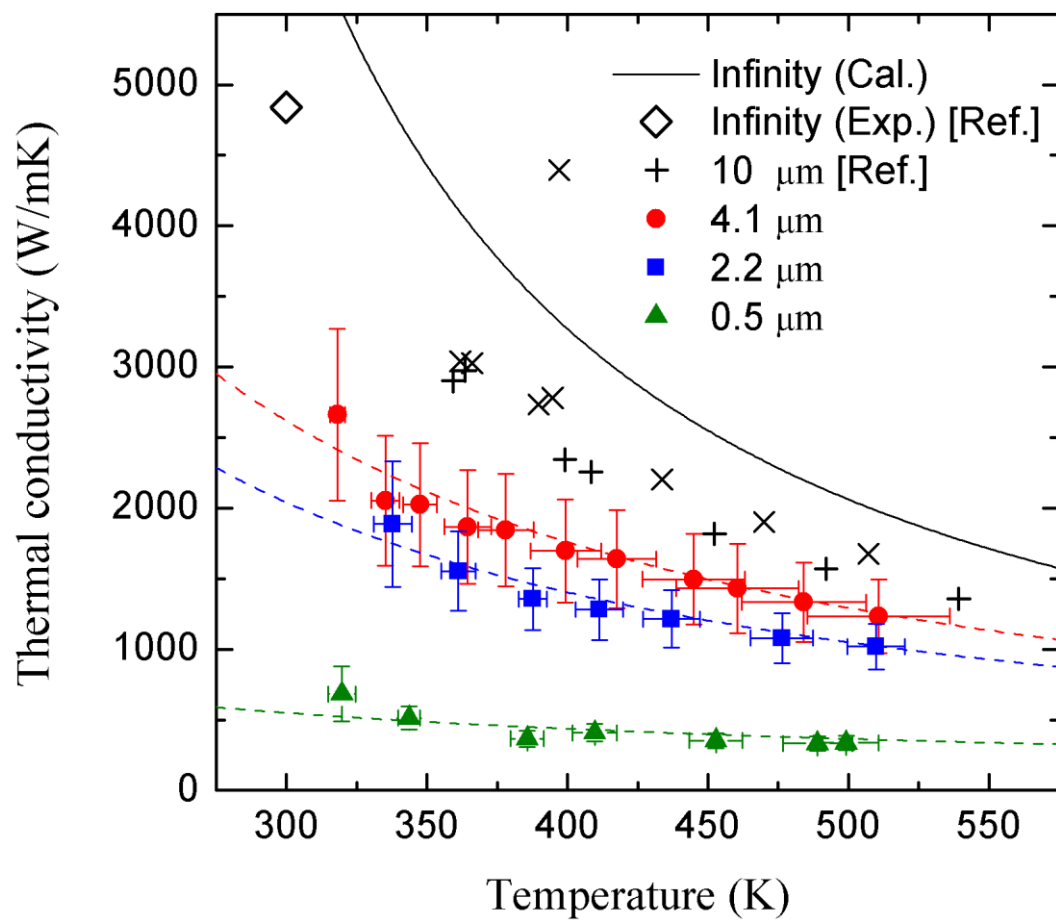
Figure 2.17 Thermal conductivity as a function of the measured temperature for the suspended graphene on the hole of 8 μm in air with grain sizes of 0.5, 2.2, and 4.1 μm

Table 2.3 Uncertainties of the measured thermal conductivities of graphene with grain sizes of 0.5, 2.2, and 4.1 μm

Grain size : 4.1 μm			Grain size : 2.2 μm			Grain size : 0.5 μm		
T	k	U_k/k	T	k	U_k/k	T	k	U_k/k
[K]	[W/mW]	[%]	[K]	[W/mW]	[%]	[K]	[W/mW]	[%]
318	2663	22.8	338	1888	23.6	320	683	28.6
335	2054	22.4	361	1554	18.1	344	513	16.3
348	2025	21.5	388	1356	16.1	386	366	16.2
364	1867	21.7	411	1282	16.8	410	109	15.4
378	1845	21.6	437	1215	16.8	453	353	14.9
399	1697	21.6	476	1079	16.3	489	332	15.1
418	1638	21.2	510	1020	15.8	499	338	14.8
445	1496	21.5						
460	1432	22.1						
484	1334	21.2	average		17.6	average		17.2
511	1234	21.2						
average		21.7						

Table 2.4 Hole edge temperature variations from the environmental temperature (T_a=300 K) and corresponding errors in thermal conductivity for the tree tested grain sizes at two different temperatures

Grain size [μm]	$T_g = 300$ K		$T_g = 500$ K	
	T_{HE} [K]	k-error [%]	T_{HE} [K]	k-error [%]
4.1	300.08	0.41	300.76	0.24
2.2	300.16	0.29	300.69	0.18
0.5	300.96	0.19	300.21	0.02
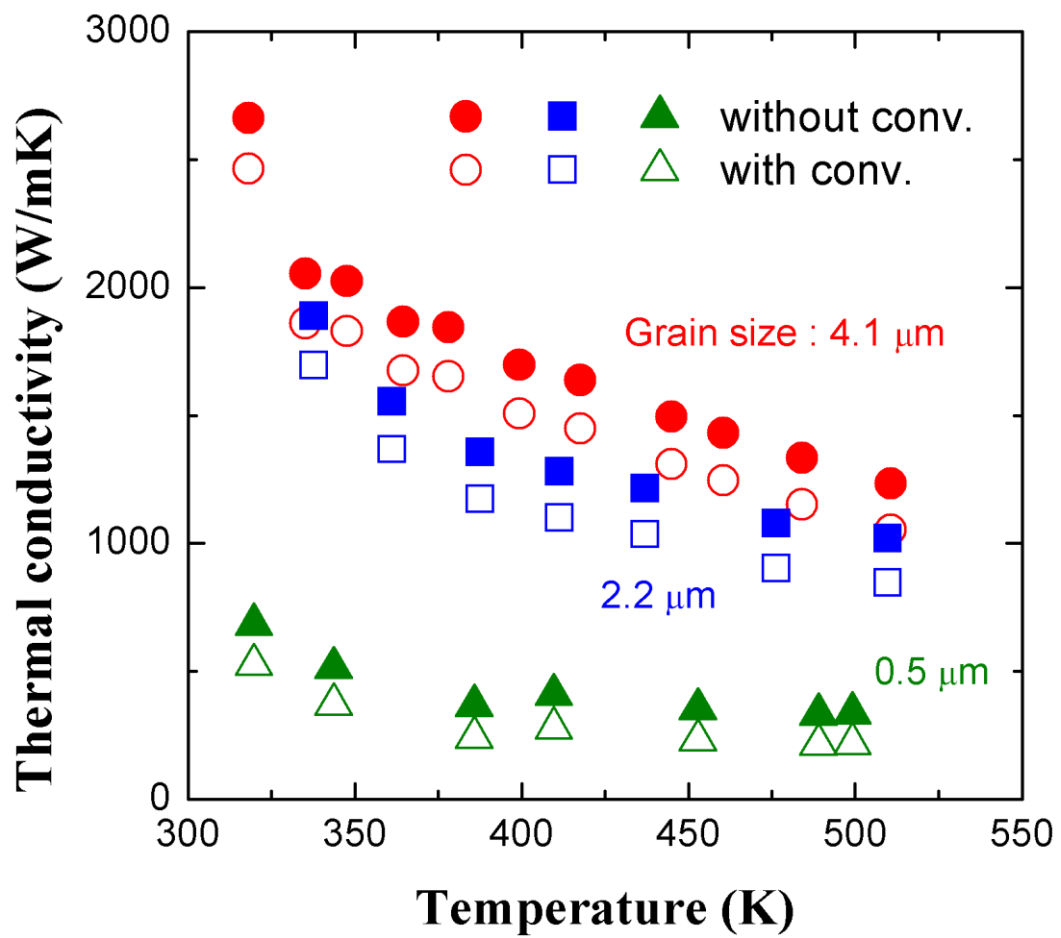
Figure 2.18 Comparison of thermal conductivities with (open mark with a dash) and without convection effect (solid) in CVD polycrystalline graphene with a grain size of 4.1, 2.2, and 0.5 μm
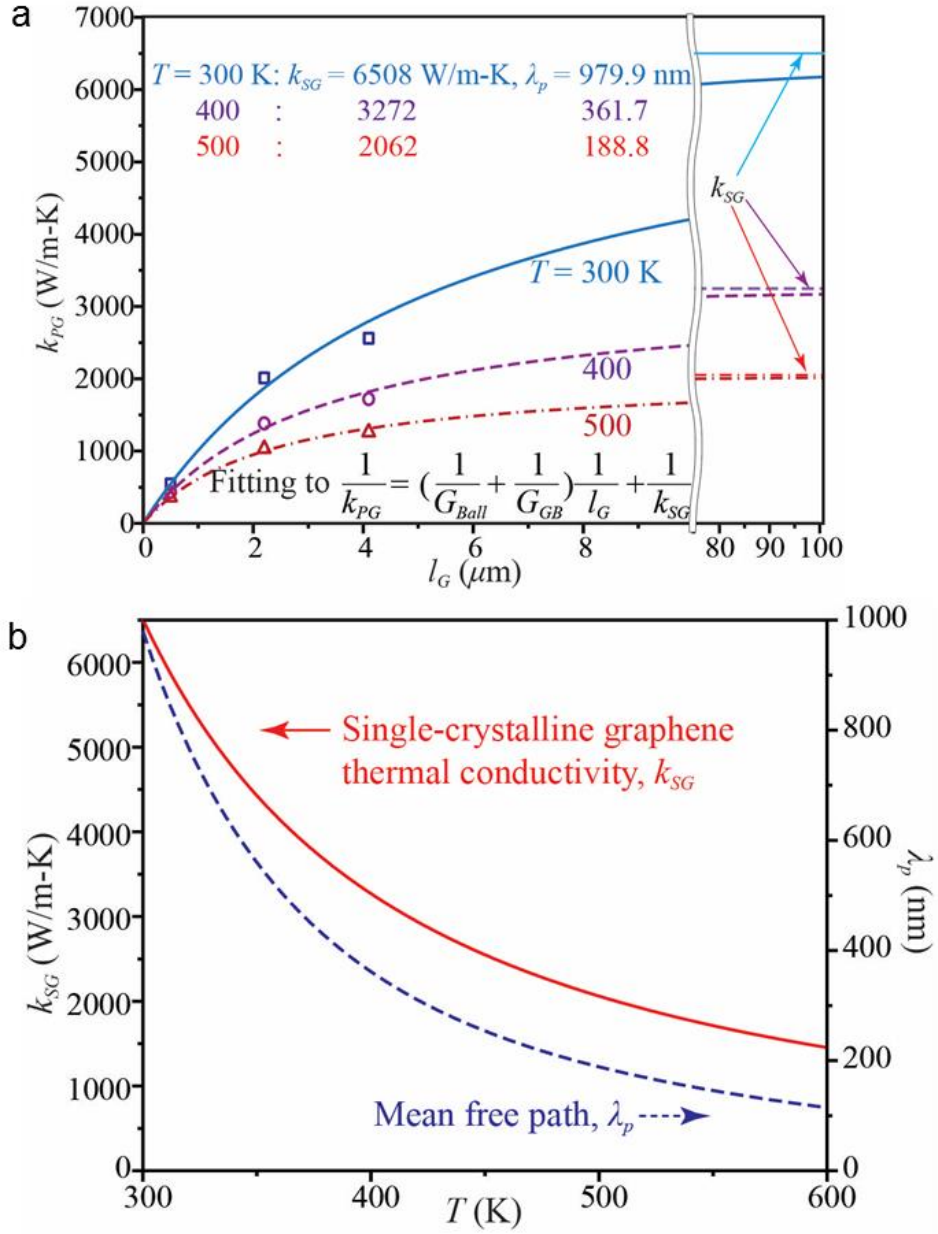
Figure 2.19 (a) Grain size dependence of polycrystalline graphene thermal conductivity at 300, 400, and 500 K (b) thermal conductivities (red solid line, left axis) and phonon mean free path (blue dashed line, right axis) of single-crystalline graphene with respect to temperature T

Table 2.5 Temperature discrepancies between T_G and T_{2D} for the tested laser power range of 3.5 to 4.5 mW

Incident laser power [mW]	T_G [K]	T_{2D} [K]	$(T_G-T_{2D})/T_{2D}$
3.5	409.8±18.3	399.3±12.6	2.63 %
4.0	436.5±21.7	417.6±14.1	4.53 %
4.5	482.6±28.5	444.9±18.2	8.47 %

Chapter 3

k Reductions of Holey Graphene as Hole-Defect Porosity

3.1 Introduction

It was experimentally confirmed that the thermal conductivity of graphene is significantly suppressed by defects, such as grain boundary. However, in recent years, some researchers have tried to reduce thermal conductivity by intentionally inducing defect in graphene sheets for applications in various fields. Therefore, in this chapter, thermal conductivity reductions of holey graphene were covered as porosity for the quantitative study of graphene thermal conductivity as defect concentrations and for the more effective thermal conductivity reductions.

At first, regular hole patterns will be fabricated by FIB processing on polycrystalline graphene with 4.1 grain sizes that was synthesizes by the established synthesis conditions in section 2.2.1. The holey graphene samples will be transferred on SiO_2 substrate with 8 nm thickness by PMMA transfer method. Then, the graphene samples will be confirmed by various technique, such as SEM, optical microscopy, and Raman spectroscopy. And porosities of holey graphene samples will be defined.

Finally, thermal conductivity reductions of holey graphene as porosity will be measured by optothermal Raman method and compared to other reference data.

3.2 Sample preparation

In this section, how to prepare HG with different porosities will be presented. Unlike the polycrystalline graphene, HG was transferred on a SiO_2 substrate to facilitate the fabrication of hole defects. Then, hole-shaped defects were fabricated in graphene sheets by FIB processing.

3.2.1 Graphene transfer (the supported graphene)

By PMMA transfer method mentioned in Section 2.2.2, HG was transferred on a transmission electron microscopy (TEM) grid of 8-nm-thick SiO_2 membranes as the supporting substrate in order to facilitate to measure thermal conductivity and fabricate the hole defects by FIB processing. The accuracy of thermal conductivity measurements can be increased by minimizing the heat dissipation to substrate of which thickness is ultra-thin (Kim et al. 2017a).

3.2.2 Fabrication of hole defects in graphene

As mentioned earlier, the quantitative study of defect effects on thermal

conductivity of defected graphene is needed. However, it is too hard to precisely control the defect sizes and concentrations in graphene.

Defects can be induced in graphene by electron beam irradiation (Malekpour et al. 2016) and oxygen plasma (Zhao et al. 2015), but the quantitative control of defects is difficult. While GNMs with the regular hole defects can be fabricated using block copolymer self-assembly (Oh et al. 2017), many concomitant processes are needed. FIB processing, which is a high-accuracy technique for nano-processing, has many advantages to induce defects on graphene sheets. The principle of FIB drilling is that the accelerated and focused ions like Ga^+ with high kinetic energy bombard atoms in the target material. As the one of the strongest points of FIB milling is that it is a direct process at the specific region, which does not require any masking or post processing,(Kim et al. 2012) we can generate various patterns effectively on graphene to tailor the local properties. Also, it is suitable for fabrication of nanopores with smooth edges in a graphene sheet with Ga^+ ions which is heavier than carbon atoms.(Li et al. 2013) Furthermore, the unexpected damages can be minimized and the amount of defects in graphene sheets can be flexibly controlled by the focused Ga^+ ions at the beam exposure points.(Liao et al. 2015) Thus, FIB milling has emerged as a promising technique for generating nanoscale patterns on graphene layer.(Zhang et al. 2014; Hemamouche et al. 2014)

The holey patterns on the graphene layer were made by using the conditions in FIB system as summarized in Table 3.1. Ga^+ ions with an acceleration energy of 30 keV and 2 pA of beam current was used. It is known that FIB process can damage at the target material during the sputtering because the Ga^+ ions can be captured in the material and cause undesired contamination, at the low ion acceleration energy.(Xu et al. 2013) However, the previous research investigating travel depth of Ga^+ ion at the epitaxial graphene concludes that the 95% Ga^+ ions stopped in 10 ~ 33 nm at the 30 keV of beam condition,(Zhang et al. 2014) and this is enough range to penetrate the graphene used in this experiment. The dwell time and number of scan were fixed as 10 μs and 500 times respectively. We used very short dwell time to avoid the unexpected lateral damage in graphene outside the irradiated area.(Liao et al. 2015) In addition, to avoid unnecessary damage on the graphene layer during the scanning for imaging, images at the target area were not captured at the entire process. In order to investigate the thermal conductivity changes of defected graphene, the center-to-center distance between hole defects were changed diversely. While the average phonon mean free path of supported graphene on SiO_2 is estimated to be ~100 nm (Pop et al. 2012), the dot-to-dot distance was controlled as 800, 400, and 200 nm in both of vertical and horizontal direction which is longer than 100 nm to observe effectively the thermal conductivity reductions of HG by suppressed the long-wavelength phonons dominantly carrying heat.

As a result, three holey graphene samples with the accurately controlled hole defects by FIB patterning process were obtained. Therefore, it is possible for the quantitative study of defect effects on thermal conductivity of graphene by analyzing and comparing the measured thermal conductivities of holey graphene samples in sequence as depicted Figure 3.1.

3.3 Characterization

The graphene sample on the substrate is characterized by various technique before conducting the main experiment. Basically, scanning electron microscopy (SEM) and optical microscopy is useful to confirm the quality of surface visually. Also, the porosity of HG is calculated. Finally, HG are characterized by Raman spectroscopy.

3.3.1 Scanning electron microscopy (SEM)

Figure 3.2 shows the HG graphene induced regular hole-defect pattern with various hole spacing. In these SEM images, 'black circles' are the hole defects fabricated by FIB processing and 'grey regions' are the CVD grown graphene. As shown in the SEM images, it is visibly confirmed that the dot-to-dot distances, in which the hole diameter is estimated about ~50 nm, are precisely controlled by the

high-accuracy FIB processing.

3.3.2 Optical microscope

Figure 3.3 shows optical images of the supported HG with different hole spacing on the SiO_2 membrane with 8-nm thickness. As shown in the optical images, graphene was transferred on the target substrate retaining enough area (red circles : ~314 μm^2) to measure thermal conductivities by the opto-thermal Raman method. It is hard to identify different hole spacing by only optical microscopy like the case of graphene with different grain sizes, so additional characterization technique is also needed.

3.3.3 Definition of porosity

Regular hole shaped defects were fabricated by FIB processing on CVD grown and transferred graphene on a SiO_2 substrate. The center-to-center distance was controlled as 0, 200, 400, 800 nm in both of vertical and horizontal direction as depicted in Figure 3.4. Therefore, porosities of HG samples can be defined by $(\pi d^2 / L_h^2) \times 100$ where d is hole diameter of 50 nm and L_h is the hole spacing of ∞, 800, 400, 200 nm, so the calculated porosities of graphene were 0, 0.31, 1.23, and 4.91 %.

3.3.5 Raman spectroscopy

HG samples were also observed by Raman spectroscopy as depicted in Figure 3.5. Raman spectra of pristine graphene (black line in Figure 3.5) shows sharp $2D$ peak without D peak, which indicates that graphene sample is defect-free and monolayer (Dresselhaus et al. 2010; Ferrari and Basko 2013a; Ferrari 2007b). As hole spacing become narrower, the intensity of D peak is more pronounced due to increase of defect density (Cançado et al. 2011b). On the other hand, $2D$ peak intensity affected by electron-hole scattering (Venezuela et al. 2011) considerably drops because increase of defects has negative effect on the electron lifetime (Eckmann et al. 2012). The enhanced D peak with decreasing $2D$ peak after FIB processing is consistent to previous studies (Liao et al. 2015; Thissen et al. 2015).

3.4 k measurements of holey graphene

When obtaining thermal conductivities of the suspended polycrystalline graphene, the simple analytic solution (Equation 2.1) was used to ignore the convection loss from graphene surface to air. However, thermal conductivity of holey graphene will be obtained by solving the full energy balance of heat diffusion for the case of the supported holey graphene on SiO_2 substrate. In this chapter, the process how to obtain thermal conductivity of holey graphene will be presented in

detail. Finally, the measured thermal conductivity reductions of holey graphene as porosity will be compared to other reference both experimental data and calculation results.

3.4.1 Heat diffusion equation

When the absorbed heat from laser is dominantly conducted along graphene sheets due to very thin and low thermal conductivity of SiO_2 substrate (Figure 3.6), the heat diffusion equation in the cylindrical coordinate of the supported grpahene is given by:

$$k_{sup}t\frac{1}{r}\frac{d}{dr}\left(r\frac{dT}{dr}\right)-2h(T-T_a)+q''(r)=0 \qquad (3.1)$$

where k_{sup} is the thermal conductivity of supported graphene, t is the graphene thickness of 0.335 nm, T_a is the ambient temperature, h is the convection heat transfer coefficient from graphene to air of 2.9×10^4 W/m^2K (Chen et al. 2010), and $q''(r)=q_0''\exp(-2r^2/r_0^2)$ is the Gaussian distribution of incident laser energy flux. The laser beam radius r_0 is estimated by $r_0=\Lambda/(\pi\cdot NA)=0.218$ µm and the peak absorbed power at the center of beam spot q_0'' is determined from $2(aQ)/\pi r_0^2$ in that α is the optical absorption of graphene Q is the total power. With the

boundary conditions of $\left.\dfrac{dT}{dr}\right|_{r=0} = 0$ and $T(\infty) = T_a$, the thermal conductivity of

graphene is determined from considering the experimentally measured temperature

is equal to the Gaussian average temperature of numerically solved $T(r)$, i.e.,

$$T_{m\_\exp} \simeq \int_0^\infty T(r)\exp\left(-\frac{2r^2}{r_0^2}\right)r\,dr \Big/ \int_0^\infty \exp\left(-\frac{2r^2}{r_0^2}\right)r\,dr = T_{m\_cal} \qquad (3.2)$$

where T_{m_exp} is the measured temperature by optothermal Raman method.

The whole process how to obtain the thermal conductivity of graphene is

summarized in Figure 3.7. The graphene temperature can be easily measured by the

linear relation between temperature and Raman $2D$ peak position. We should find

the true thermal conductivity by trial and error. When the calculated temperature by

Equation 3.2 is equal to the measured temperature by experiment, the thermal

conductivity is correct.

3.4.2 Optical absorption of graphene

When measuring optical absorption of graphene for the case of supported

graphene, substrate effect should be considered unlike the case of the suspended

graphene. In order to measure the optical absorption of graphene samples from laser

irradiation, both the reflection and the transmission through the graphene-on-SiO_2

and the bare SiO_2 were observed as in Figure 3.8. In both detections, the absolute

pixel intensity of the image or the power read from the power meter doesn't tell us

the reflectance (Re_g and Re_{SiO2}) or transmittance (Tr_g and Tr_{SiO2}) directly. Instead,

the ratios of reflection (Re_g/Re_{SiO2}) and transmission (Tr_g/Tr_{SiO2}) bear meaningful

information for the determination of the optical absorption of graphene, and they

are defined as ρ and τ, respectively (Figure 3.8). From simple analytical calculations

by using Fresnel's equations and transfer matrix method (or multiple reflection

inside the thin transparent SiO_2 layer), the values Re_{SiO2} and Tr_{SiO2} are readily given.

These values and the measured ratios ρ and τ, can determine the optical absorption

of graphene a_g from a basic relationship, $a_g=1-Re_g-Tr_g=1-\rho Re_{SiO2}-\tau Tr_{SiO2}$. The

measured optical absorption ranges from 0.0314 (=3.14%) to 0.0319 (=3.19%),

showing no distinct differences between graphene samples.

3.4.3 The correlation between 2D peak positions and temperature

For the case of holey graphene with hole defects, the same results of the linear

temperature dependence of Raman 2D peak shift as the hot plate temperature was

observed as shown in Figure 3.9. The temperature coefficients are $d\omega/dT =$-

0.0276, -0.033, -0.0339, and -0.0385 cm^{-1}/K for the hole spacing of 200, 400, 800,

and infinity nm, respectively. The measured correlation of Raman 2D peak

positions and temperature will be used to determine the graphene temperature

heated by Raman laser in optothermal Raman technique.

3.4.4 The temperature rises as the absorbed laser power

For the case of graphene with different hole spacing, the similar linear dependences are observed as shown in Figure 3.10. As hole spacing decreases, the defect density increases in the unit area. Therefore, the absorbed heat from Raman laser is not effectively transported through the holey graphene with smaller hole spacing. As a result, the measured temperature of graphene with small hole spacing is higher than that with large hole spacing in Figure 3.10.

3.4.5 k reductions of holey graphene as porosity

For the case of the supported HG with different porosities, the thermal conductivities can be obtained from Equation 3.1. For a better insight, the reductions of thermal conductivities with porosity variations are compared in Figure 3.11. The measured thermal conductivities of HG distinctly decrease for the range of porosity from 0 to 4.91 %. As porosity increases, the thermal conductivities of graphene declined to 20 % for 4.91 % porosity. Hole defects induce additional phonon-defect scattering by imperfect lattice structure (Nika and Balandin 2012) and phonon relaxation time is inverse proportional to defect concentrations (Klemens and Pedraza 1994; Zhang et al. 2011), which reduces phonon mean free

path of HG. Therefore, high porosity ultimately results in lowered the thermal conductivity of HG. The thermal conductivities of GNMs (triangle symbols in Figure 3.11) with the averaged porosity of ~34 and ~45 % were reduced to 18.3 and 10.6 %, respectively (Oh et al. 2017). And the thermal conductivity of defected (green dash-dot line in Figure 3.12) by oxygen plasma was decreased to 4.6 % for the oxygen-containing defects concentrations of ~0.66 %.(Zhao et al. 2015) As a result, the thermal conductivity of HG by FIB processing is effectively suppressed comparing to the thermal conductivity reductions of GNM and defected graphene as depicted in Figure 3.11.

As the same method, uncertainties of the measured thermal conductivities of graphene with porosities of 0, 0.31, 1.23, and 4.91 % in Table 3.2. The accuracy of thermal conductivity measurements is improved by using ultra-thin substrate that minimizes the heat dissipation into substrate, ranging from ± 16 % to ± 19 %. However, the uncertainty for the case of HG with 4.91 % porosity seems relatively higher (± 58 %), because Raman $2D$ peak intensity of HG with 4.91 % porosity is too low to define the peak position by fitting to Lorentzian function.

To compare the reductions of thermal conductivity as porosity k/k_0, the reference thermal conductivity of graphene without any defects k_0 should be known for the reference value as summarized Table 3.3. The k_0 of supported graphene on SiO_2 is measured as 1045 W/mK in this study, which is consistent to the previous

result for the case of the repeated thermal annealing in ambient air.(Kim et al. 2017b) The k_0 of suspended graphene on a through hole were reported by 3170 W/mK (Oh et al. 2017) and 3500 W/mK (Zhao et al. 2015), which are used to calculate the reduction of thermal conductivity as the k_0 of GNM and defected graphene, respectively. Eucken model given by $k/k_0 = (1 - porsity)/(1 + porosity/2)$ (Eucken 1932), which is the classical model to express the thermal conductivity of bulk porous medium and valid when the system size is sufficiently larger than phonon MFP of the medium, doesn't need the k_0 to calculate the thermal conductivity reductions. The k_0 of supported graphene on SiO_2 is estimated as ~1011 W/mK by fitting of thermal model based on the MFPAF in this study, showing very low difference to experiment result under 0.03 % error. The k_0 of PG was calculated as ~782 W/mK by molecular dynamics (MD) calculation (Nobakht et al. 2017). This value is much smaller than the measured thermal conductivities of pristine graphene by experiment due to the limitation of domain size in MD calculation, so perfectly calculating the quantitative thermal conductivity of graphene is hard by MD simulation.

Meanwhile, the reduction rate of thermal conductivities decreases as porosity increases. The hole defects serve as scattering centers for the delocalized long-wavelength phonons (Noshin et al. 2017; Malekpour et al. 2016), but phonon scattering rate of the delocalized modes is substantially small compared to that of

the short-ranged localized modes due to shortened phonon MFP at high defect density (Malekpour et al. 2016). Hence, the results of the measured thermal conductivities of graphene show a fast decrease at low porosity and then a gradual decay at high porosity. The fitting results of thermal model developed in this study based on MFPAF show good agreement with the experimental results (red line in Figure 3.11 and thermal model will be further described later). The molecular dynamics simulations of GNM also demonstrated that the reduction rate of thermal conductivities decreases with increasing porosity (blue dash line in Figure 3.12) (Nobakht et al. 2017). On the other hand, Eucken model (black dot line in Figure 3.11) shows the linear reductions of thermal conductivities as porosity. And unlike the modified model and MD simulation, there are large discrepancies between experimental data and Eucken model. It represents that Eucken model has a limitation to predict the reduction of thermal conductivity as porosity for the HG having the nm-size of hole spacing comparable to phonon MFP.

3.5 Conclusion

For the quantitative study of defect effects on thermal transport in graphene, the holey patterns on the graphene sheet are precisely produced by FIB technique, so HG with various porosities are prepared by controlling the hole spacing as 0, 200,

400, and 800 nm. HG samples were supported on ultra-thin SiO_2 membrane with 8 nm thickness in order to minimize the heat dissipation into the substrate. The porosities of HG were defined as 0, 0.31, 1.23, and 4.91 %.

HG with porosity of 0, 0.31, 1.23, and 4.1 % shows significant thermal conductivity reductions with increasing porosity. In particular, the thermal conductivity of HG is suppressed to 20 % for 4.91 % porosity compared to that of graphene without hole defects. The results of this study show that the thermal conductivity of graphene can be locally and flexibly controlled by FIB processing and provide fundamental information of thermal transport in the defected graphene.

Table 3.1 The conditions of FIB pattering process

Condition	Value
Acceleration voltage (keV)	30
Probe current (pA)	1
Dwell time (μs)	10
Number of scan (times)	500
Center-to-center distance (nm)	200, 400, 800
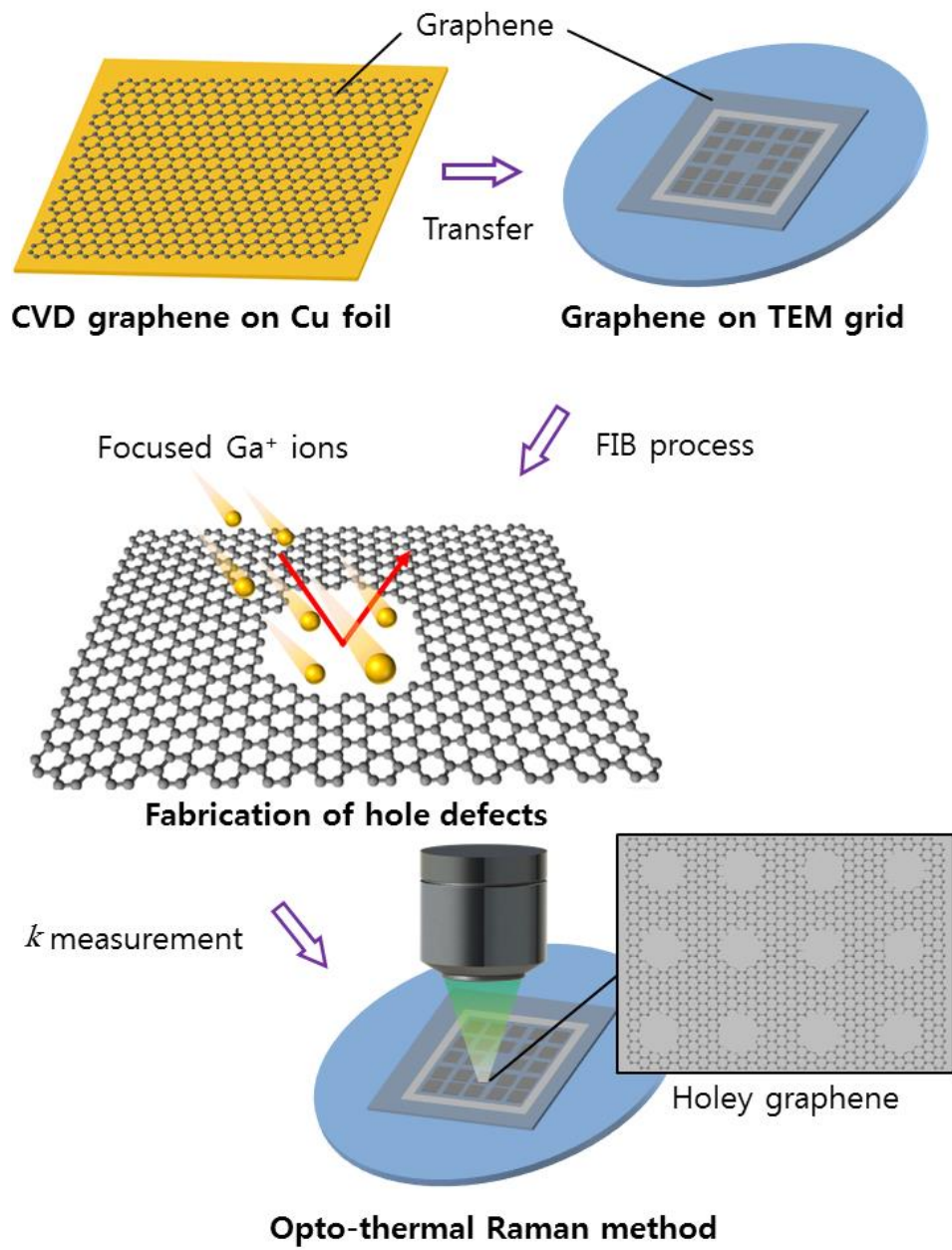
Figure 3.1 Schematic of sample preparation and experiment process about HG
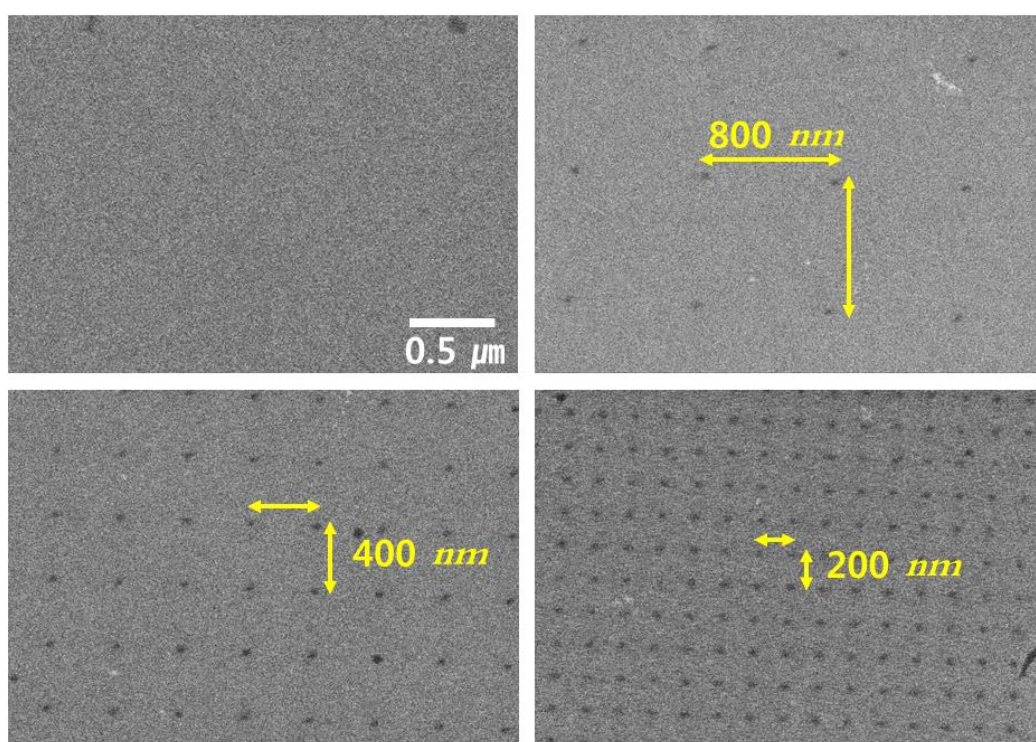
Figure 3.2 SEM images of graphene without hole defects and HG with hole spacing of 800, 400, and 200 nm
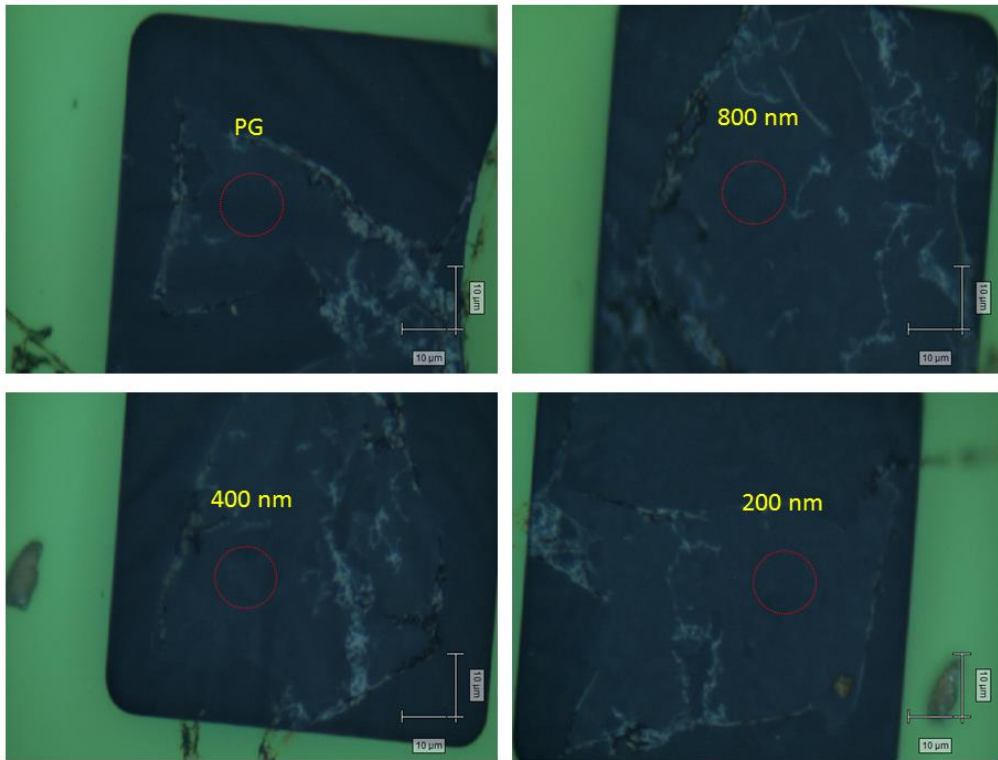
Figure 3.3 Optical images of the supported HG with different hole spacing on the SiO$_2$ membrane with 8-nm thickness
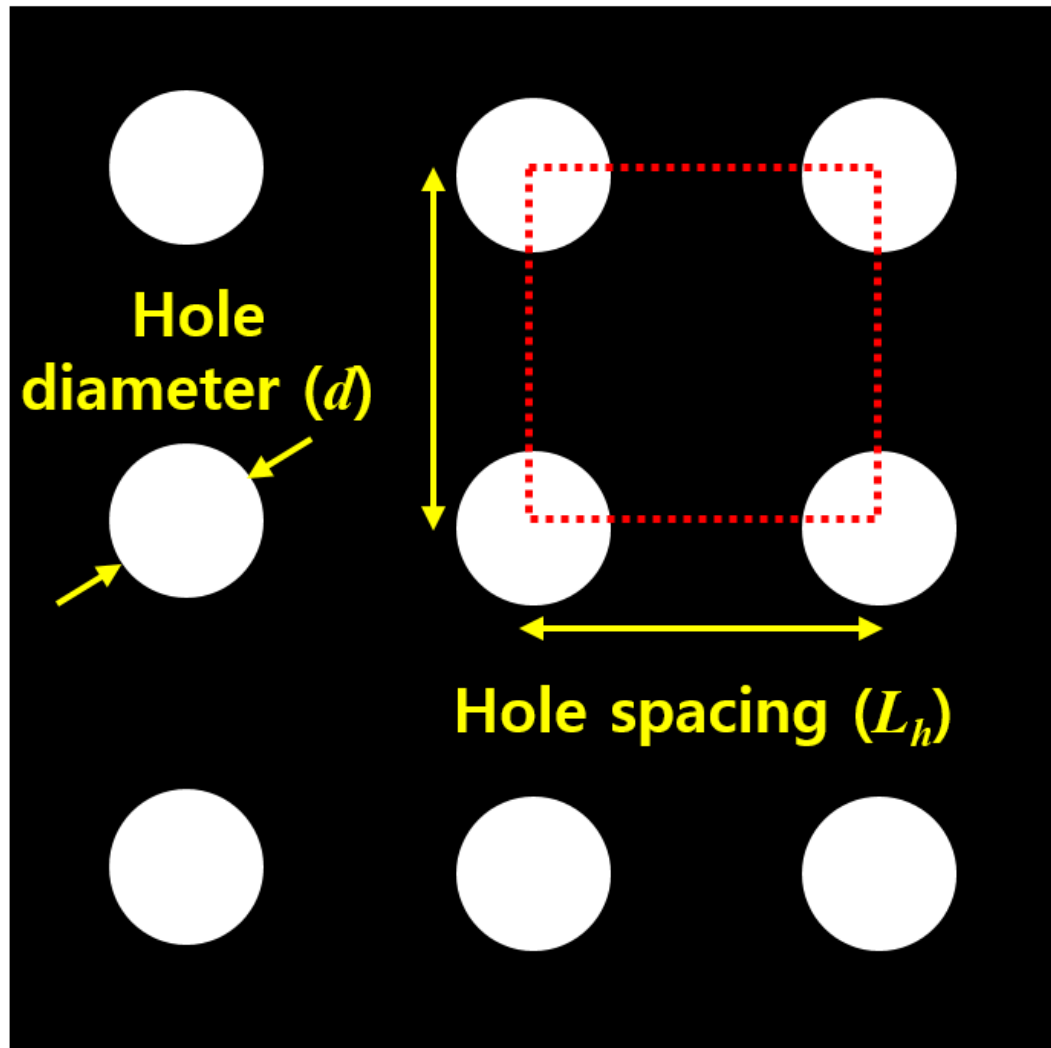
Figure 3.4 The schematic of hole patterns in holey graphene
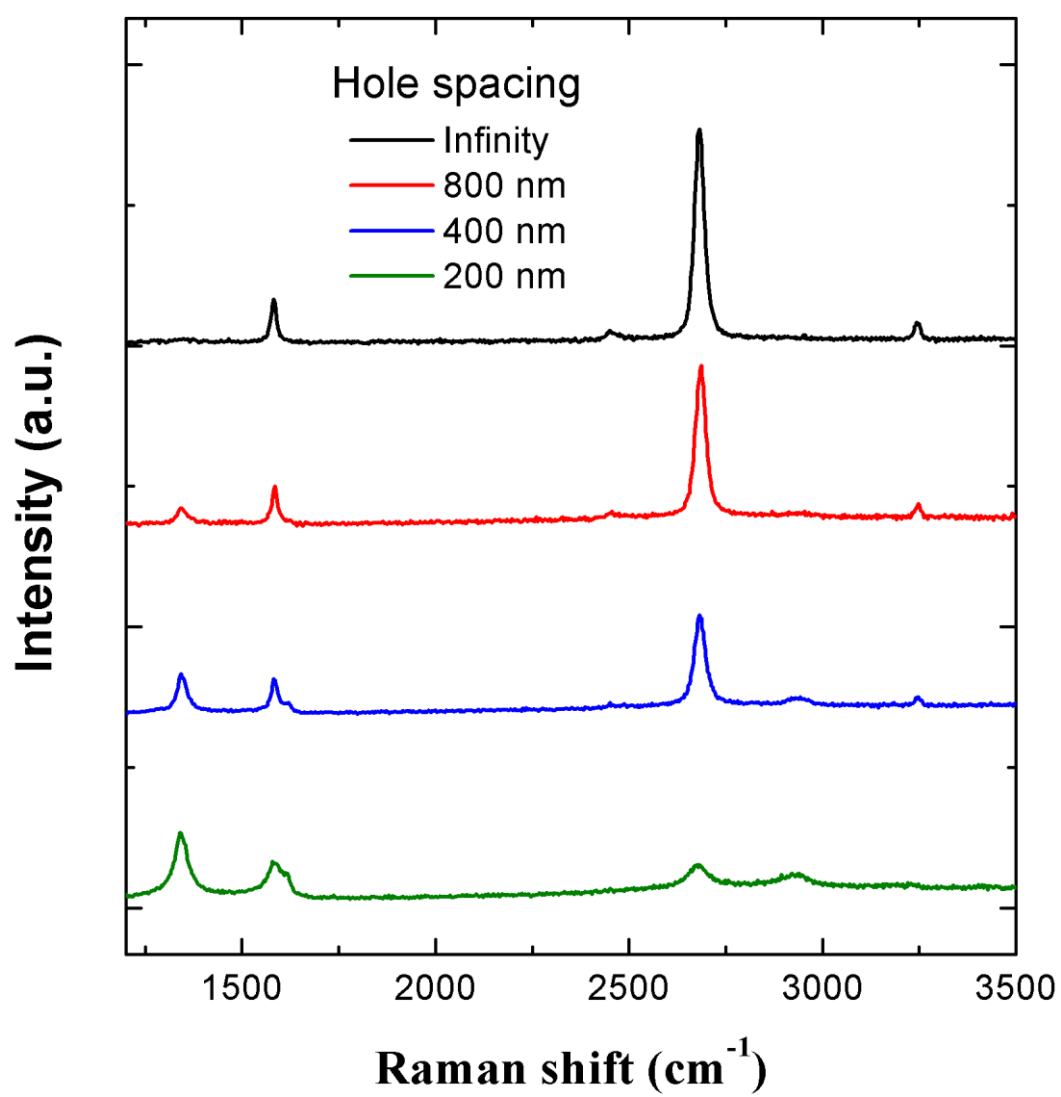
Figure 3.5 Raman spectra of graphene with different hole spacing of infinity, 800, 400, and 200 nm
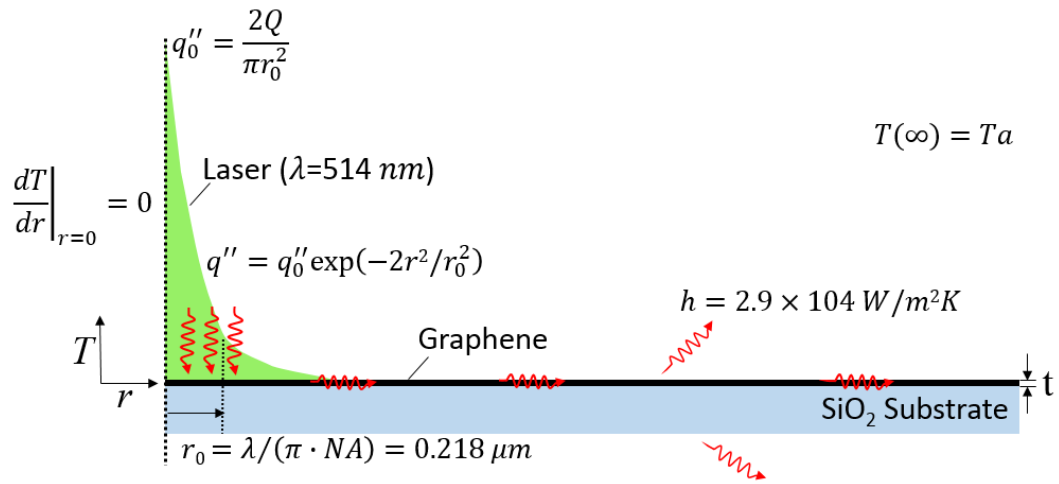
Figure 3.6 Schematic illustration of the supported graphene on SiO2 substrate with 8-nm thickness

Calculation

Experiment

Give a k

Measure the relationship between 2D Raman and temperature dw_{2D}/dT

Obtain the temperature profile by Solving the energy balance equation $T(r)$

Measure the 2D peak shift by laser Δw_{2D}

Calculate the temperature

$$T_{m\_cal} = \frac{\int_0^\infty T(r) exp\left(-\frac{2r^2}{r_0^2}\right) r dr}{\int_0^\infty exp\left(-\frac{2r^2}{r_0^2}\right) r dr}$$

Calculate the temperature

$$T_{m\_exp} = 300\ K + \frac{\Delta w_{2D}}{dw_{2D}/dT}$$

Change k

$T_{m\_cal} = T_{m\_exp}$?

no

yes

Correct k
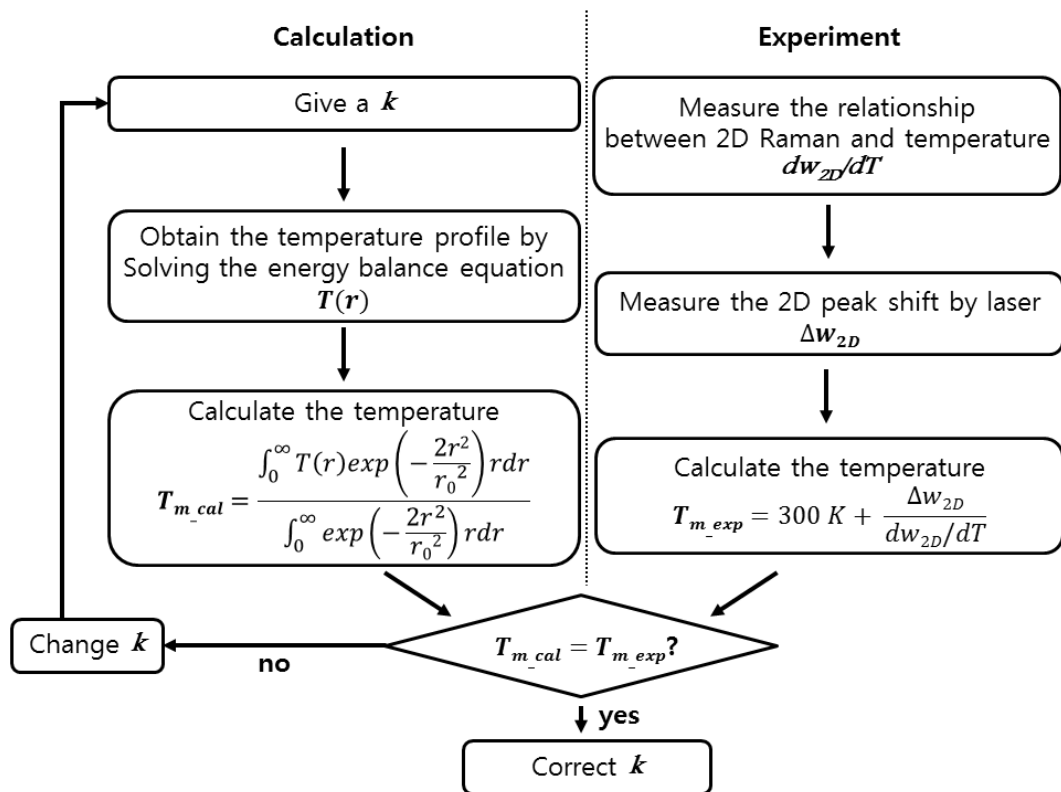
Figure 3.7 The process how to obtain the thermal conductivity of graphene
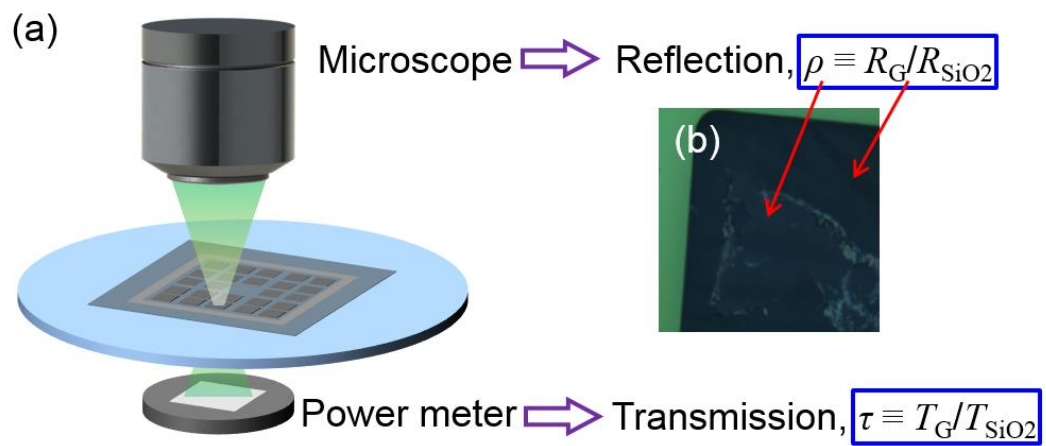
Figure 3.8 (a) Schematic illustration of measuring reflection by microscope and (b) an image of measuring reflection in order to obtain the optical absorption of supported graphene on SiO2 substrate
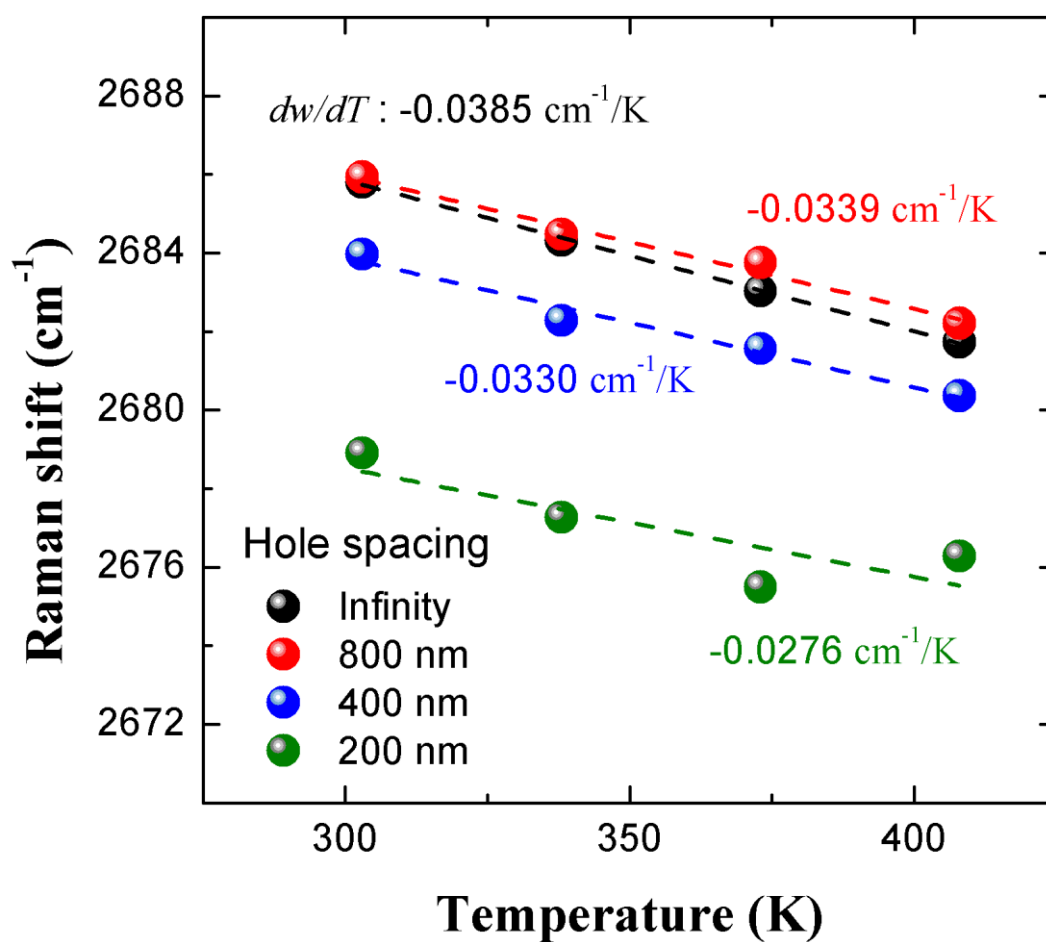
Figure 3.9 The correlation between the 2*D* peak positions and the hot plate temperature of graphene with hole spacing of 200, 400, 800 and infinity nm
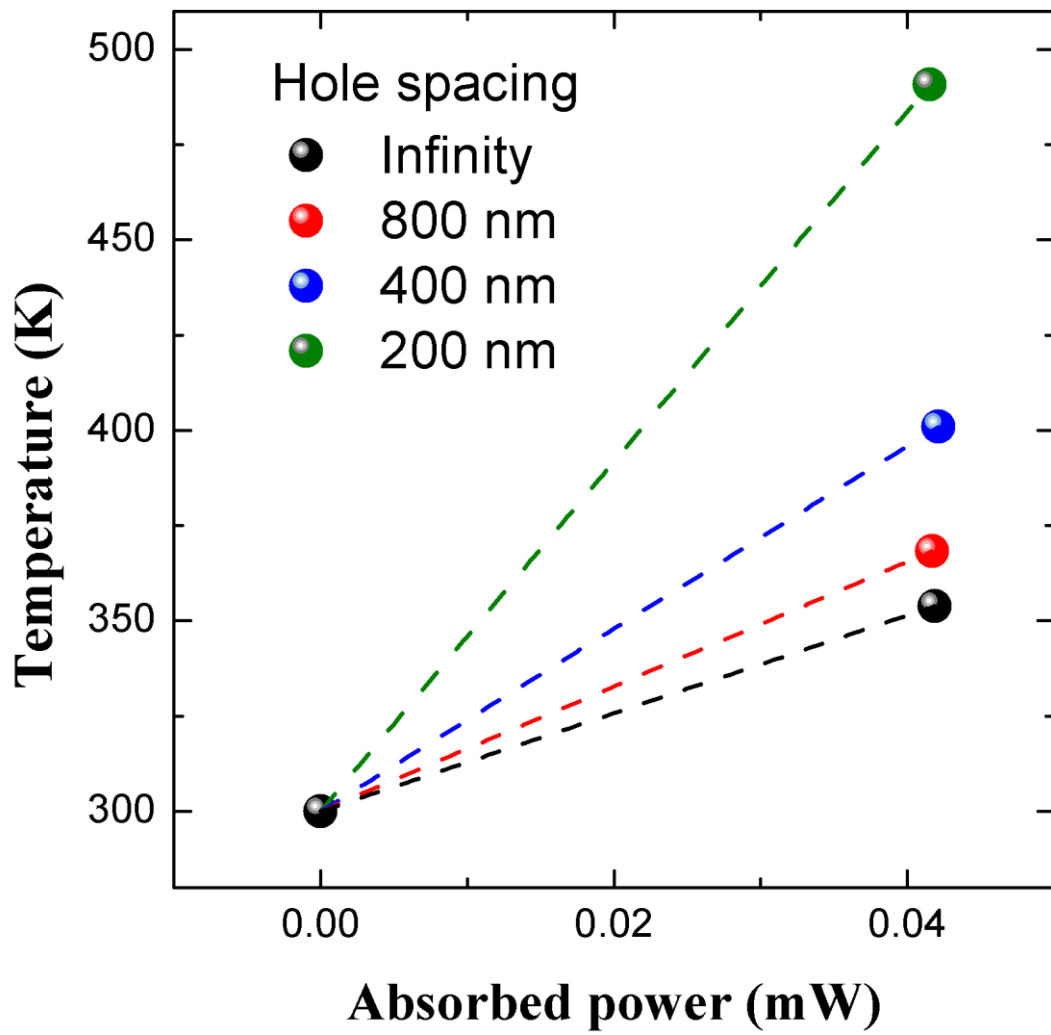
Figure 3.10 The measured temperature rises as the absorbed laser power increases for each graphene with hole spacing of 200, 400, 800, and infinity nm
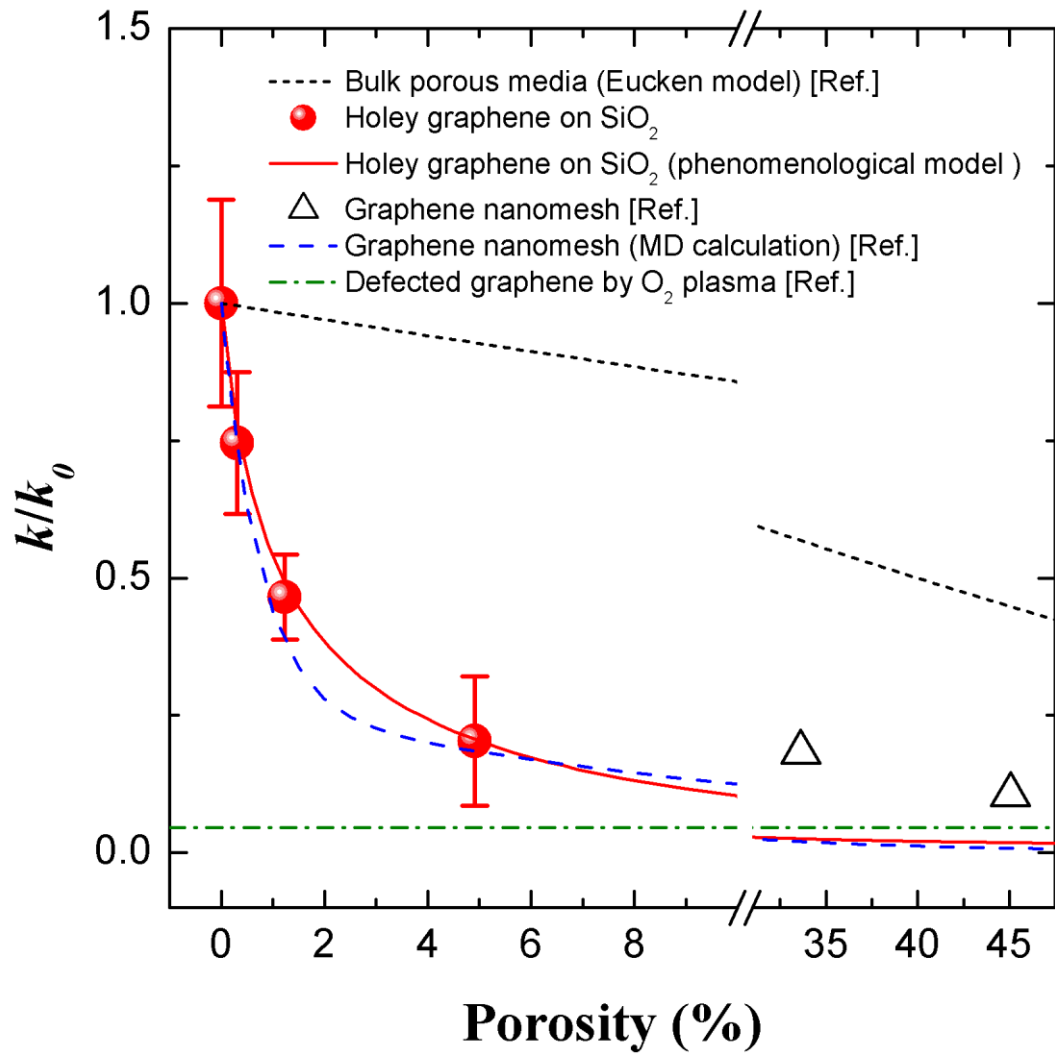
Figure 3.11 Thermal conductivity reductions as a function of the porosities for the supported graphene with 0, 0.31, 1.23, and 4.91 % porosity

Table 3.2 Uncertainties of the measured thermal conductivities of graphene with porosities of 0, 0.31, 1.23, and 4.91 %

Porosity [%]	k [W/mK]	k/k_0	U_k/k [%]
0	1045	1	18.8
0.31	779	0.75	17.3
1.23	486	0.47	16.6
4.91	212.6	0.20	57.6

Table 3.3 Summary of the reference thermal conductivity of graphene (k_0) for thermal conductivity reductions

Reference	Method	Sample	k_0 (W/mK)	Remarks
Present work	Optothermal Raman	Supported graphene	1045	Pristine graphene supported on SiO_2
	Thermal model		1014	The fitting result based on the MFPAF
Zhao, *et al.* [14]	Optothermal Raman	Suspended graphene	3500	Pristine graphene suspended on a through hole
Oh, *et al.* [15]			3170	
Eucken, A. [34]	Eucken model		-	Only valid in the sufficiently larger system size than phonon MFP of materials
Nobakht, *et al.* [35]	MD calculation		782	Small k_0 due to size limitation of MD calculation

Chapter 4

Summary and Conclusions

The thermal conductivities of suspended graphene with grain sizes of 0.5, 2.2, 4.1 μm were measured in order to figure out the grain boundary effects on thermal transport in polycrystalline CVD graphene by optothermal Raman method. And thermal conductivity reductions of the supported HG with porosities of 0, 0.31, 1.23, 4.91 % were measured for the quantitative study of thermal conductivity as defects concentrations.

In Chapter 2, it was covered about grain boundary effects on thermal transport in polycrystalline CVD graphene. By analyzing the complicated relations between synthesis conditions in CVD systems, new synthesis conditions for graphene with different grain sizes were established. 3 graphene samples with different grain sizes were characterized by various technique, such as SEM, optical microscopy, Raman spectroscopy after transferring on the target substrate by PMMA transfer method. Also, the average grain sizes of polycrystalline graphene were defined as 0.5, 2.2, and 4.1 μm by MDA and digital image processing. Then, thermal conductivities were measured by optothermal Raman method. At first, optical absorption and the correlation between 2D peak positions and temperature of graphene were measured. Then, the temperature rises were also measured as the absorbed laser power. Finally,

the thermal conductivities of graphene samples were obtained by solving the heat diffusion equation. As a result, the thermal conductivities of suspended graphene with different grain sizes were reduced as grain sizes decrease. Especially, the thermal conductivity reduction of graphene with grain sizes of 0.5 μm that is smaller than phonon mean free path of suspended graphene (~775 nm) was distinct. Furthermore, various analyses were conducted to supplement the experimental results. Uncertainties of the measured thermal conductivities are estimated by root-sum-square method and uncertainties of all graphene samples were about ±20 %. By numerically solving the full energy balance, the hole edge temperature of suspended graphene and the convection effect were calculated. The calculation results show that the assumption that the graphene temperature at the hole edge is equal to ambient temperature is valid and the air convection loss can be ignored. Also, the thermal conductivities of single-crystal graphene were estimated by a simple chain model showing a good agreement with the experimental data. Finally, NE effect was confirmed by comparing temperature discrepancies between T_G and T_{2D}.

In Chapter 3, thermal conductivity reductions of HG as porosity were measured and compared to other reference data. HG samples with different porosities were fabricated by FIB processing. The porosities of HG were calculated as 0, 0.31, 1.23, and 4.91 % by using the hole-defect diameter and hole spacing. In case of the holey

graphene, the thermal conductivities were also reduced as porosities increase.

In this thesis, the thermal conductivity data of suspended graphene with different grain sizes are firstly reported. It will help to understand the grain boundary effect on thermal transport in polycrystalline graphene grown by CVD method. Also, the quantitative study of graphene thermal conductivity as hole-defect concentrations (porosity) is conducted, in which regular hole shaped defects can be fabricated by FIB processing. The thermal conductivities of holey graphene are significantly decreased as porosity increases, which represents the thermal conductivity of holey graphene can be locally tailored by delicately fabricating the hole defects at the specific region.

References

Bae, M.-H., Z. Li, Z. Aksamija, P. N. Martin, F. Xiong, Z.-Y. Ong, I. Knezevic, and E. Pop. 2013. Ballistic to diffusive crossover of heat flow in graphene ribbons. *Nature communications* 4:1734.

Balandin, A. A. 2011. Thermal properties of graphene and nanostructured carbon materials. *Nature materials* 10 (8):569-581.

Balandin, A. A., S. Ghosh, W. Bao, I. Calizo, D. Teweldebrhan, F. Miao, and C. N. Lau. 2008. Superior thermal conductivity of single-layer graphene. *Nano Letters* 8 (3):902-907.

Banhart, F., J. Kotakoski, and A. V. Krasheninnikov. 2010. Structural defects in graphene. *ACS nano* 5 (1):26-41.

Berciaud, S., S. Ryu, L. E. Brus, and T. F. Heinz. 2008. Probing the intrinsic properties of exfoliated graphene: Raman spectroscopy of free-standing monolayers. *Nano Letters* 9 (1):346-352.

Berger, C., Z. Song, X. Li, X. Wu, N. Brown, C. Naud, D. Mayou, T. Li, J. Hass, and A. N. Marchenkov. 2006. Electronic confinement and coherence in patterned epitaxial graphene. *science* 312 (5777):1191-1196.

Bolotin, K. I., K. Sikes, Z. Jiang, M. Klima, G. Fudenberg, J. Hone, P. Kim, and H. Stormer. 2008. Ultrahigh electron mobility in suspended graphene. *Solid state communications* 146 (9):351-355.

Bonini, N., M. Lazzeri, N. Marzari, and F. Mauri. 2007. Phonon anharmonicities in graphite and graphene. *Physical Review Letters* 99 (17):176802.

Cahill, D. G., P. V. Braun, G. Chen, D. R. Clarke, S. Fan, K. E. Goodson, P.

Keblinski, W. P. King, G. D. Mahan, and A. Majumdar. 2014. Nanoscale thermal transport. II. 2003–2012. *Applied Physics Reviews* 1 (1):011305.

Cahill, D. G., K. Goodson, and A. Majumdar. 2002. Thermometry and thermal transport in micro/nanoscale solid-state devices and structures. *Journal of Heat Transfer* 124 (2):223-241.

Cai, W., A. L. Moore, Y. Zhu, X. Li, S. Chen, L. Shi, and R. S. Ruoff. 2010. Thermal transport in suspended and supported monolayer graphene grown by chemical vapor deposition. *Nano Letters* 10 (5):1645-1651.

Calizo, I., F. Miao, W. Bao, C. Lau, and A. Balandin. 2007. Variable temperature Raman microscopy as a nanometrology tool for graphene layers and graphene-based devices. *Applied physics letters* 91 (7):071913.

Cançado, L. G., A. Jorio, E. M. Ferreira, F. Stavale, C. Achete, R. Capaz, M. Moutinho, A. Lombardo, T. Kulmala, and A. Ferrari. 2011a. Quantifying defects in graphene via Raman spectroscopy at different excitation energies. *Nano Letters* 11 (8):3190-3196.

Cançado, L. G., A. Jorio, E. Martins Ferreira, F. Stavale, C. Achete, R. Capaz, M. Moutinho, A. Lombardo, T. Kulmala, and A. Ferrari. 2011b. Quantifying defects in graphene via Raman spectroscopy at different excitation energies. *Nano Letters* 11 (8):3190-3196.

Celebi, K., M. T. Cole, K. B. Teo, and H. G. Park. 2011. Observations of early stage graphene growth on copper. *Electrochemical and Solid-State Letters* 15 (1):K1-K4.

Chen, S., Q. Li, Q. Zhang, Y. Qu, H. Ji, R. S. Ruoff, and W. Cai. 2012a. Thermal conductivity measurements of suspended graphene with and without wrinkles by micro-Raman mapping. *Nanotechnology* 23 (36):365701.

Chen, S., A. L. Moore, W. Cai, J. W. Suk, J. An, C. Mishra, C. Amos, C. W.

Magnuson, J. Kang, and L. Shi. 2010. Raman measurements of thermal transport in suspended monolayer graphene of variable sizes in vacuum and gaseous environments. *ACS nano* 5 (1):321-328.

Chen, S., Q. Wu, C. Mishra, J. Kang, H. Zhang, K. Cho, W. Cai, A. A. Balandin, and R. S. Ruoff. 2012b. Thermal conductivity of isotopically modified graphene. *Nature materials* 11 (3):203-207.

Dresselhaus, M. S., A. Jorio, M. Hofmann, G. Dresselhaus, and R. Saito. 2010. Perspectives on carbon nanotubes and graphene Raman spectroscopy. *Nano Letters* 10 (3):751-758.

Eckmann, A., A. Felten, A. Mishchenko, L. Britnell, R. Krupke, K. S. Novoselov, and C. Casiraghi. 2012. Probing the nature of defects in graphene by Raman spectroscopy. *Nano Letters* 12 (8):3925-3930.

Eres, G., M. Regmi, C. M. Rouleau, J. Chen, I. N. Ivanov, A. A. Puretzky, and D. B. Geohegan. 2014. Cooperative island growth of large-area single-crystal graphene on copper using chemical vapor deposition. *ACS nano* 8 (6):5657-5669.

Eucken, A. 1932. Thermal conductivity of ceramics refractory materials. *Forsch. Geb. Ing., B-3, Forschungsheft* 53:6-21.

Faugeras, C., B. Faugeras, M. Orlita, M. Potemski, R. R. Nair, and A. Geim. 2010. Thermal conductivity of graphene in corbino membrane geometry. *ACS nano* 4 (4):1889-1892.

Feng, T., X. Ruan, Z. Ye, and B. Cao. 2015. Spectral phonon mean free path and thermal conductivity accumulation in defected graphene: The effects of defect type and concentration. *Physical Review B* 91 (22):224301.

Ferrari, A. 1824. Phys. Re V. B 2001, 64, 75414.(b) Carlo Ferrari, A.; Robertson. *Philos. Trans. R. Soc. London, Ser. A* 2004:362.

Ferrari, A. C. 2007a. Raman spectroscopy of graphene and graphite: disorder, electron–phonon coupling, doping and nonadiabatic effects. *Solid state communications* 143 (1-2):47-57.

———. 2007b. Raman spectroscopy of graphene and graphite: disorder, electron–phonon coupling, doping and nonadiabatic effects. *Solid state communications* 143 (1):47-57.

Ferrari, A. C., and D. M. Basko. 2013a. Raman spectroscopy as a versatile tool for studying the properties of graphene. *Nature nanotechnology* 8 (4):235-246.

———. 2013b. Raman spectroscopy as a versatile tool for studying the properties of graphene. *Nature nanotechnology* 8 (4):235.

Ghosh, S., I. Calizo, D. Teweldebrhan, E. Pokatilov, D. Nika, A. Balandin, W. Bao, F. Miao, and C. Lau. 2008a. Extremely high thermal conductivity of graphene: Prospects for thermal management applications in nanoelectronic circuits. *Applied Physics Letters* 92 (15):151911.

Ghosh, S., I. Calizo, D. Teweldebrhan, E. P. Pokatilov, D. L. Nika, A. A. Balandin, W. Bao, F. Miao, and C. N. Lau. 2008b. Extremely high thermal conductivity of graphene: Prospects for thermal management applications in nanoelectronic circuits. *Applied physics letters* 92 (15):151911.

Gilje, S., S. Han, M. Wang, K. L. Wang, and R. B. Kaner. 2007. A chemical route to graphene for device applications. *Nano Letters* 7 (11):3394-3398.

Hemamouche, A., A. Morin, E. Bourhis, B. Toury, E. Tarnaud, J. Mathé, P. Guégan, A. Madouri, X. Lafosse, and C. Ulysse. 2014. FIB patterning of dielectric, metallized and graphene membranes: A comparative study. *Microelectronic Engineering* 121:87-91.

Jang, W., W. Bao, L. Jing, C. Lau, and C. Dames. 2013. Thermal conductivity of

suspended few-layer graphene by a modified T-bridge method. *Applied physics letters* 103 (13):133102.

Jang, W., Z. Chen, W. Bao, C. N. Lau, and C. Dames. 2010. Thickness-dependent thermal conductivity of encased graphene and ultrathin graphite. *Nano Letters* 10 (10):3909-3913.

Jeong, C., S. Datta, and M. Lundstrom. 2011. Full dispersion versus Debye model evaluation of lattice thermal conductivity with a Landauer approach. *Journal of Applied Physics* 109 (7):073718.

Jiang, J., R. Saito, G. G. Samsonidze, A. Jorio, S. Chou, G. Dresselhaus, and M. Dresselhaus. 2007. Chirality dependence of exciton effects in single-wall carbon nanotubes: Tight-binding model. *Physical Review B* 75 (3):035407.

Kaviany, M. 2014. *Heat transfer physics*: Cambridge University Press.

Kim, C.-S., S.-H. Ahn, and D.-Y. Jang. 2012. Developments in micro/nanoscale fabrication by focused ion beams. *Vacuum* 86 (8):1014-1035.

Kim, H. G., K. D. Kihm, W. Lee, G. Lim, S. Cheon, W. Lee, K. R. Pyun, S. H. Ko, and S. Shin. 2017a. Effect of graphene-substrate conformity on the in-plane thermal conductivity of supported graphene. *Carbon* 125:39-48.

———. 2017b. Effect of graphene-substrate conformity on the in-plane thermal conductivity of supported graphene. *Carbon*.

Kim, K. S., Y. Zhao, H. Jang, S. Y. Lee, J. M. Kim, K. S. Kim, J.-H. Ahn, P. Kim, J.-Y. Choi, and B. H. Hong. 2009. Large-scale pattern growth of graphene films for stretchable transparent electrodes. *Nature* 457 (7230):706-710.

Klemens, P., and D. Pedraza. 1994. Thermal conductivity of graphite in the basal plane. *Carbon* 32 (4):735-741.

Lai, S., S. Kyu Jang, Y. Jae Song, and S. Lee. 2014. Probing graphene defects and estimating graphene quality with optical microscopy. *Applied physics letters* 104 (4):043101.

Larciprete, R., S. Ulstrup, P. Lacovig, M. Dalmiglio, M. Bianchi, F. Mazzola, L. Hornekær, F. Orlando, A. Baraldi, and P. Hofmann. 2012. Oxygen switching of the epitaxial graphene–metal interaction. *ACS nano* 6 (11):9551-9558.

Lee, C., X. Wei, J. W. Kysar, and J. Hone. 2008. Measurement of the elastic properties and intrinsic strength of monolayer graphene. *science* 321 (5887):385-388.

Lewis, A. M., B. Derby, and I. A. Kinloch. 2013. Influence of gas phase equilibria on the chemical vapor deposition of graphene. *ACS nano* 7 (4):3104-3117.

Li, W., L. Liang, S. Zhao, S. Zhang, and J. Xue. 2013. Fabrication of nanopores in a graphene sheet with heavy ions: A molecular dynamics study. *Journal of applied physics* 114 (23):234304.

Li, X., W. Cai, J. An, S. Kim, J. Nah, D. Yang, R. Piner, A. Velamakanni, I. Jung, and E. Tutuc. 2009. Large-area synthesis of high-quality and uniform graphene films on copper foils. *science* 324 (5932):1312-1314.

Li, X., C. W. Magnuson, A. Venugopal, J. An, J. W. Suk, B. Han, M. Borysiak, W. Cai, A. Velamakanni, and Y. Zhu. 2010. Graphene films with large domain size by a two-step chemical vapor deposition process. *Nano Letters* 10 (11):4328-4334.

Liao, Z., T. Zhang, M. Gall, A. Dianat, R. Rosenkranz, R. Jordan, G. Cuniberti, and E. Zschech. 2015. Lateral damage in graphene carved by high energy focused gallium ion beams. *Applied physics letters* 107 (1):013108.

Malekpour, H., P. Ramnani, S. Srinivasan, G. Balasubramanian, D. L. Nika, A. Mulchandani, R. K. Lake, and A. A. Balandin. 2016. Thermal conductivity of

graphene with defects induced by electron beam irradiation. *Nanoscale* 8 (30):14608-14616.

Mingo, N., and D. Broido. 2005. Carbon nanotube ballistic thermal conductance and its limits. *Physical Review Letters* 95 (9):096105.

Moffat, R. J. 1988. Describing the uncertainties in experimental results. *Experimental thermal and fluid science* 1 (1):3-17.

Munoz, E., J. Lu, and B. I. Yakobson. 2010. Ballistic thermal conductance of graphene ribbons. *Nano Letters* 10 (5):1652-1656.

Nair, R. R., P. Blake, A. N. Grigorenko, K. S. Novoselov, T. J. Booth, T. Stauber, N. M. Peres, and A. K. Geim. 2008. Fine structure constant defines visual transparency of graphene. *science* 320 (5881):1308-1308.

Nihira, T., and T. Iwata. 2003. Temperature dependence of lattice vibrations and analysis of the specific heat of graphite. *Physical Review B* 68 (13):134305.

Nika, D., E. Pokatilov, A. Askerov, and A. Balandin. 2009. Phonon thermal conduction in graphene: Role of Umklapp and edge roughness scattering. *Physical Review B* 79 (15):155413.

Nika, D. L., and A. A. Balandin. 2012. Two-dimensional phonon transport in graphene. *Journal of Physics: Condensed Matter* 24 (23):233203.

Nika, D. L., E. P. Pokatilov, and A. A. Balandin. 2011. Theoretical description of thermal transport in graphene: The issues of phonon cut-off frequencies and polarization branches. *physica status solidi (b)* 248 (11):2609-2614.

Nobakht, A. Y., S. Shin, K. D. Kihm, D. C. Marable, and W. Lee. 2017. Heat flow diversion in supported graphene nanomesh. *Carbon* 123:45-53.

Noshin, M., A. I. Khan, I. A. Navid, H. A. Uddin, and S. Subrina. 2017. Impact of

vacancies on the thermal conductivity of graphene nanoribbons: A molecular dynamics simulation study. *AIP Advances* 7 (1):015112.

Novoselov, K. S., A. K. Geim, S. V. Morozov, D. Jiang, Y. Zhang, S. V. Dubonos, I. V. Grigorieva, and A. A. Firsov. 2004. Electric field effect in atomically thin carbon films. *science* 306 (5696):666-669.

Oh, J., H. Yoo, J. Choi, J. Y. Kim, D. S. Lee, M. J. Kim, J.-C. Lee, W. N. Kim, J. C. Grossman, and J. H. Park. 2017. Significantly reduced thermal conductivity and enhanced thermoelectric properties of single-and bi-layer graphene nanomeshes with sub-10nm neck-width. *Nano Energy* 35:26-35.

Pettes, M. T., I. Jo, Z. Yao, and L. Shi. 2011. Influence of polymeric residue on the thermal conductivity of suspended bilayer graphene. *Nano Letters* 11 (3):1195-1200.

Pimenta, M., G. Dresselhaus, M. S. Dresselhaus, L. Cancado, A. Jorio, and R. Saito. 2007. Studying disorder in graphite-based systems by Raman spectroscopy. *Physical chemistry chemical physics* 9 (11):1276-1290.

Pop, E., V. Varshney, and A. K. Roy. 2012. Thermal properties of graphene: Fundamentals and applications. *MRS bulletin* 37 (12):1273-1281.

Prasher, R. 2008. Thermal boundary resistance and thermal conductivity of multiwalled carbon nanotubes. *Physical Review B* 77 (7):075424.

Rego, L. G., and G. Kirczenow. 1998. Quantized thermal conductance of dielectric quantum wires. *Physical Review Letters* 81 (1):232.

Saito, R., A. Jorio, A. Souza Filho, G. Dresselhaus, M. Dresselhaus, and M. Pimenta. 2001. Probing phonon dispersion relations of graphite by double resonance Raman scattering. *Physical review letters* 88 (2):027401.

Schedin, F., A. Geim, S. Morozov, E. Hill, P. Blake, M. Katsnelson, and K.

Novoselov. 2007. Detection of individual gas molecules adsorbed on graphene. *Nature materials* 6 (9):652-655.

Seol, J. H., I. Jo, A. L. Moore, L. Lindsay, Z. H. Aitken, M. T. Pettes, X. Li, Z. Yao, R. Huang, and D. Broido. 2010. Two-dimensional phonon transport in supported graphene. *science* 328 (5975):213-216.

Seol, J. H., A. L. Moore, L. Shi, I. Jo, and Z. Yao. 2011. Thermal conductivity measurement of graphene exfoliated on silicon dioxide. *Journal of Heat Transfer* 133 (2):022403.

Serov, A. Y., Z.-Y. Ong, and E. Pop. 2013. Effect of grain boundaries on thermal transport in graphene. *Applied physics letters* 102 (3):033104.

Shin, S., and M. Kaviany. 2011. Interflake thermal conductance of edge-passivated graphene. *Physical Review B* 84 (23):235433.

Singh, D., J. Y. Murthy, and T. S. Fisher. 2011. Spectral phonon conduction and dominant scattering pathways in graphene. *Journal of Applied Physics* 110 (9):094312.

Sullivan, S., A. Vallabhaneni, I. Kholmanov, X. Ruan, J. Murthy, and L. Shi. 2017. Optical generation and detection of local non-equilibrium phonons in suspended graphene. *arXiv preprint arXiv:1701.03011*.

Tewary, V. K., and B. Yang. 2009. Singular behavior of the Debye-Waller factor of graphene. *Physical Review B* 79 (12):125416.

Thissen, N. F., R. Vervuurt, J. Mulders, J. Weber, W. Kessels, and A. Bol. 2015. The effect of residual gas scattering on Ga ion beam patterning of graphene. *Applied physics letters* 107 (21):213101.

Tohei, T., A. Kuwabara, F. Oba, and I. Tanaka. 2006. Debye temperature and stiffness of carbon and boron nitride polymorphs from first principles calculations.

Physical Review B 73 (6):064304.

Vallabhaneni, A. K., D. Singh, H. Bao, J. Murthy, and X. Ruan. 2016. Reliability of Raman measurements of thermal conductivity of single-layer graphene due to selective electron-phonon coupling: A first-principles study. *Physical Review B* 93 (12):125432.

Venezuela, P., M. Lazzeri, and F. Mauri. 2011. Theory of double-resonant Raman spectra in graphene: Intensity and line shape of defect-induced and two-phonon bands. *Physical Review B* 84 (3):035433.

Wang, H., and M. Sen. 2009. Analysis of the 3-omega method for thermal conductivity measurement. *International Journal of Heat and Mass Transfer* 52 (7-8):2102-2109.

Wang, Y., Z. Song, and Z. Xu. 2014. Characterizing phonon thermal conduction in polycrystalline graphene. *Journal of Materials Research* 29 (3):362-372.

Wu, P., S. Quek, Z. Sha, Z. Dong, X. Liu, G. Zhang, Q. Pei, and Y. Zhang. 2014. Thermal transport behavior of polycrystalline graphene: A molecular dynamics study. *Journal of applied physics* 116 (20):204303.

Xu, Y., K. Zhang, C. Brüsewitz, X. Wu, and H. C. Hofsäss. 2013. Investigation of the effect of low energy ion beam irradiation on mono-layer graphene. *AIP Advances* 3 (7):072120.

Yang, H.-S., G.-R. Bai, L. Thompson, and J. Eastman. 2002. Interfacial thermal resistance in nanocrystalline yttria-stabilized zirconia. *Acta Materialia* 50 (9):2309-2317.

Zhang, H., G. Lee, and K. Cho. 2011. Thermal transport in graphene and effects of vacancy defects. *Physical Review B* 84 (11):115460.

Zhang, Y., C. Hui, R. Sun, K. Li, K. He, X. Ma, and F. Liu. 2014. A large-area 15

nm graphene nanoribbon array patterned by a focused ion beam. *Nanotechnology* 25 (13):135301.

Zhao, W., Y. Wang, Z. Wu, W. Wang, K. Bi, Z. Liang, J. Yang, Y. Chen, Z. Xu, and Z. Ni. 2015. Defect-engineered heat transport in graphene: a route to high efficient thermal rectification. *Scientific reports* 5:11962.

결정 경계와 구멍 결함에 의한
다결정 CVD 그래핀의 열전도도 감소

서울대학교 대학원

기계항공공학부

이 우 민

요 약

탄소 원자들로 구성된 2차원 물질인 그래핀은 높은 전기적 이동도, 광학적 투명성, 뛰어난 강성 등 우수한 물리적 성질들 때문에 엄청난 주목을 받고 있다. 특히, 그래핀은 2차원 구조에서 비롯된 긴 포논 평균 자유행로 때문에 예외적으로 뛰어난 열 물성을 가지고 있다. 그래핀의 이례적으로 높은 열전도도는 결정 경계, 공격자점, 외부 원자와 같은 결함들에 의해 현저하게 감소 될 수 있다. 그러므로 많은 결정 경계를 가지고 있는 다결정 구조의 CVD 그래핀에서 결정 경계가 열전달에 미치는 영향에 대해 반드시 연구가 필요하다.

본 연구에서는 다결정 그래핀에서 결정 경계가 열전달에 미치는 영

향을 연구하기 위해 화학적 증기 증착법을 이용하여 결정 크기가 다른 그래핀 샘플을 합성 하였다. 화학적 증기 증착 합성 조건들의 조절은 제어된 결정 크기를 가지는 단층의 다결정 그래핀 합성이 가능하게 했다. 3가지 다른 결정 크기를 가지는 그래핀의 열전도도는 라만 스펙트럼에서 온도 의존적인 2D 피크 이동을 이용하는 광열 라만 분광법에 의해 측정 되었다. 우선 라만 레이저 조사로 결함 있는 그래핀이 흡수한 파워를 정의하기 위해 광학적 흡수율을 측정 하였다. 그 다음 라만 2D 피크의 온도 계수와 흡수된 파워에 따른 2D 피크 이동이 측정 되었다. 최종적으로 측정된 실험 데이터를 열확산 방정식에 대입하여 풀이함으로써 결함 있는 그래핀의 열전도도를 도출 하였다. 더 나아가, 완전한 에너지 평형을 수치적을 계산함으로써 공기 대류 손실에 의한 효과와 매달린 그래핀의 구멍 가장자리의 온도를 분석 하였다. 실험 데이터들의 보외법 및 피팅을 통해 단결정 그래핀의 열전도도를 추정 하였다. 그리고 포논들의 비평형을 확인 하기 위해 라만 G 피크와 2D 피크 이동으로 각각 측정된 온도 사이에 차이를 비교 하였다.

비록 그래핀 안에 결함들이 그래핀 열전도도에 나쁜 영향을 미치지만 결함을 이용하여 그래핀의 열전도도를 억제는 다양한 응용분야에 적용하기 위해 유용할 수 있다. 결함 농도에 따른 그래핀의 열전도도에 대한 정량적 연구와 더욱 효과적인 열전도도 억제를 위해, 다공성 정도에 따른 구멍 뚫린 그래핀의 열전도도 저감을 대해 광열 라만 분광법을

이용하여 측정하였다. 그러한 연구를 위해 집속이온빔 공정으로 구멍 뚫린 그래핀을 확보 하였다. 구멍 결함들은 어떠한 마스킹 또는 후공정이 필요 없는 직접적인 집속이온빔 공정을 통해 정확하게 가공 및 제어 되었다. 그래핀 샘플들이 PMMA를 이용하여 기판 위에 전사된 후에 라만 분광, SEM, 광학 현미경 등 다양한 방법을 통해 분석 하였다. 마침내, 다공성 정도에 따른 구멍 뚫린 그래핀의 측정된 열전도도 감소는 다른 참고 실험 및 계산 결과들과 비교 되었다.

주요어 : 열전도도, CVD 그래핀, 광열 라만 분광법, 결정 경계, 구멍 뚫린 그래핀

학 번 : 2013-20696